# Picosecond acoustics: a new way to access elastic properties of materials at pressure and temperature conditions of planetary interiors

Silvia Boccato, Michel Gauthier, Nicki C. Siersch, Paraskevas Parisiades, Yiuri Garino, Simon Ayrinhac, Sofia Balugani, Cécile Bretonnet, Thibault Delétang, Maëva Guillot, et al.

# Picosecond acoustics: a new way to access elastic properties of materials at pressure and temperature conditions of planetary interiors.

Silvia Boccato[1*], Michel Gauthier[1], Nicki C. Siersch[1], Paraskevas Parisiades[1], Yiuri Garino[1], Simon Ayrinhac[1], Sofia Balugani[1,2], Cécile Bretonnet[1], Thibault Delétang[1,3], Maëva Guillot[1], Katia Verbeke[1], Frédéric Decremps[1], Yoann Guarnelli[1], Marc Morand[1], Philippe Rosier[1,4], Bin Zhao[1] and Daniele Antonangeli[1]

[1]Institut de Minéralogie de Physique des Matériaux et de Cosmochimie (IMPMC), Sorbonne Université, Muséum National d'Histoire Naturelle, CNRS UMR 7590, 75005 Paris, France.
[2]Present address: ESRF European Synchrotron Radiation Facility, 38000 Grenoble, France.
[3]Present address: Institut des Nanosciences de Paris (INSP), Sorbonne Université, CNRS UMR 7588, 75005 Paris, France.
[4]Present address: Laboratoire de Physique des 2 Infinis Irène Joliot-Curie (IJCLab), Université Paris-Saclay, CNRS UMR 9012, 91405 Orsay, France.

*Corresponding author(s). E-mail(s): silvia.boccato@upmc.fr;

**Abstract**

Picosecond acoustics is an optical pump-probe technique allowing to access thermoelastic properties and sound velocities of a large variety of materials under extreme conditions. Coupled with diamond anvil cells and laser heating, picosecond acoustic measurements offer the possibility to probe materials over a pressure and temperature range directly pertinent for the deep planetary interiors. In this paper we highlight the capabilities and versatility of this technique by presenting some recent applications on materials of geophysical interest. All the independent components of the elastic tensor of MgO are simultaneously determined

by measurements on single crystal at ambient conditions. Compressional sound velocity is measured at high pressure on an iron-carbon alloy and on polycrystalline argon. First laser heating test measurements performed on molybdenum at high pressure are also presented. These examples demonstrate that picosecond acoustics is a valuable alternative to already existing techniques for determining the physical properties of samples under extreme pressure and temperature conditions.

**Keywords:** Picosecond Acoustics, High Pressure, Laser Heating, Planetary interior, Sound velocity, Brillouin, MgO, Fe-C, Argon, Molybdenum

# 1 Introduction

Knowledge of the elastic properties and sound wave velocities as a function of pressure and temperature of materials constituting planetary interiors is key for the interpretation of seismic observations, providing the necessary link between seismological, mineralogical and compositional models. Thanks to the development of ultrafast pulsed lasers and their commercial availability, picosecond acoustics is an advanced but accessible technique for determining the thermoelastic properties, in a laboratory setup, of several materials, including materials of interest for geophysics, condensed matter physics and biology.

Picosecond acoustics is an optical pump-probe method that exploits time-resolved reflectivity measurements to study the propagation of acoustic waves in a large variety of samples, such as crystalline or amorphous solids, be these single- or poly-crystals, and liquids, irrespective of their optical and electronic properties (e.g. opaque or transparent materials, metals or insulators, magnetic or not). In addition to time of flight measurements, analogous in many aspects to the classical ultrasonic pulse-echo technique (see [1] for a review paper on applications of ultrasonic interferometry at high pressure), picosecond acoustics allows phonon surface imaging as a function of time [2], and time-resolved stimulated Brillouin scattering measurements, thus including applications generally covered by classic Brillouin spectroscopy (see [3] for a review paper of application of Brillouin scattering in geoscience and [4]). Since its invention in 1984 [5] this technique has been extended to measurements at high pressure and high temperature and used to experimentally determine elastic constants, sound velocities and equations of state (EOS). Recently, 3D-echography imaging measurements of samples in a diamond anvil cell (DAC) have also been reported [6].

Up to now, picosecond acoustic has been used at ambient temperature and high pressure conditions up to 150 GPa on polycrytalline samples compressed in a DAC measuring the sound velocities of Fe [7], $H_2$ [8], Fe-Ni alloys [9] and Fe-Si alloys [10, 11]. Measurements on single crystals allowed determining the complete elastic tensor of Si up to 8 GPa [2]. Simultaneous high pressure and

high temperature conditions were reached by resistively heated DAC (RH-DAC), up to 10 GPa and $\sim$ 600 K, investigating the sound velocities and EOS of liquid Hg [12, 13] as well as the melting curve and thermodynamic properties of liquid Ga [14], Rb [15] and Cs [16].

The above examples, and the ones we provide later on, clearly highlight the capability and versatility of the technique. With respect to classic MHz pulse-echo ultrasonic technique, picosecond acoustics allows measurements on much thinner samples, of the order of hundreds of nm to few tens of microns, thus being compatible with experimentation in DAC at Mbar pressures. Differently from Brillouin spectroscopy, picosecond acoustics is not limited to optically transparent samples, and data with much higher signal to noise ratio can be obtained in much shorter time (seconds to minutes), more compatible with extreme thermodynamic conditions difficult to maintain stable for long period. Noteworthy, measurements do not suffer from contribution from diamonds, and the signal can be easily corrected (when needed) for contribution coming from the pressure-transmitting medium. Over the past years, synchrotron-based techniques have been implemented and are now currently used (see [17] for a review of measurements on hcp-Fe). However, besides the intrinsically limited access to third generation synchrotron sources (which practically affects the type and number of studies), both inelastic X-ray scattering (IXS) and nuclear resonant inelastic scattering (NRIXS) suffer some limitations, mostly deriving from the fact that none of these techniques directly measure sound velocity. NRIXS probes the partial projected phonon density of states of materials having a Mössbauer isotope, and measurements are limited to the aggregate velocities (e.g. [18, 19]). IXS measures the momentum-resolved phonon dispersion and can in principle be applied to any material, does not require any equation of state, and is capable of probing polycrystals (e.g. [20–23]) as well as single crystals (e.g. [24–26]), but data analysis and interpretation in the case of polycrystalline sample (as the case for experiments at Mbar pressure) critically depends on how close to the linear part of the phonon dispersion data can be collected, and on the knowledge of sample texture. For both techniques typical uncertainties on sound velocity determination are of the order of few percent, larger than conventional ultrasonic methods.

Extreme conditions of pressure and temperature are potentially attainable as well by ns pump and probe laser ultrasonics. With the pump and the probe laser focalized of the same side on the sample, ns laser ultrasonics allows to measure both bulk waves and skimming waves, as demonstrated in Chigarev et al. for the case of iron up to 23.3 GPa [27]. This technique has been also exploited to measure skimming waves on a one-side laser heated iron sample, but the strong thermal gradients in the sample did not allow to determine the bulk waves with a reliable metrology [28]. Laser ultrasonics thus overcomes some of the critical aspects of the above-described techniques, e.g. being compatible with opaque polycrystalline samples loaded in a diamond anvil cell. However, to the best of our knowledge, further work is needed to make this

setup compatible with a double-sided laser heating, and cannot be used yet to measure bulk sound velocities at temperatures of few thousands of Kelvin.

With these premises, being able to extend applications of picosecond acoustic to further higher pressure and temperature conditions, in the Mbar range and at several thousands of K, offers the possibility of measuring sound velocities and estimating densities of planetary materials over conditions that allow a direct comparison with the reference seismological model such as PREM [29] for the center of the Earth. Moreover, the determination of melting curves of planetary materials at such extreme conditions allows placing experimental constrains on temperature profiles for planetary interiors [30, 31].

The perspective of fully exploiting the capabilities of the technique at the extreme pressures and temperatures proper to the conditions of planetary interiors called for an upgrade of the picosecond acoustics system installed at the Institut de Minéralogie Physique des Matériaux et Cosmochimie (IMPMC)[1]. One of the main upgrades of the picosecond acoustics system consisted in the addition of a laser heating system that allows to heat the sample to temperatures in the order of thousands of K [32] while being at high pressure (for reference, Earth's core-mantle boundary pressure and temperature is estimated at 130 GPa and around 4000 K, see e.g. [33]). In parallel, the control and acquisition software was object of a major upgrade to allow a faster data acquisition and consequently to gain sensitivity and accuracy, resulting in an improved data statistics and in a reduction of approximately a factor 3 in the uncertainties. Compared to the previous system, an image with comparable resolution can now be obtained eight times faster, thus reducing possible laser induced damage to the surface, which is crucial for samples with a low ablation threshold.

The new picosecond acoustics set-up was designed to simultaneously measure acoustic data, pressure and temperature. Thanks to the installation of linear actuators and the creation of an adapted software, it is now possible to visualize the sample on a camera, to switch to the collection of signal from an optical gauge for pressure determination such as ruby ($Cr:Al_2O_3$) or samarium ($SrB_4O_7:Sm^{2+}$) and to switch to temperature determination where the collected grey body radiation of the laser heated spot is fit to the Planck's law. Test measurements have been performed on different samples at different pressure and temperature conditions to evaluate the capabilities of this newly constructed system.

The paper is structured as follows.

General principles of picosecond acoustics technique are presented in Section 2, where experimental details of the system used in this work are also provided. The two measurement modes, imaging mode for the determination of the elastic constants and temporal mode for the determination of the longitudinal sound velocity, are introduced.

The first scientific example is the determination of the single-crystal elastic moduli of MgO at ambient conditions presented in Section 3. This example

[1]Sorbonne Université, CNRS UMR 7590, Paris (France)

demonstrates the possibility to experimentally measure all the components of the elastic tensor as well as the longitudinal and shear sound velocities of a relatively thick (about 100 $\mu$m) transparent sample. Being transparent, the longitudinal sound velocity can be measured along a selected crystallographic direction by using the Brillouin detection mode, with the pump laser focused on an optic coupler (a sub-micrometric layer of Al in the present case) and the probe laser spatially aligned on the pump. Thanks to the deposition of an optic coupler on both sides of the sample, the intersection of the propagating acoustic wavefront with the sample surface at the probe side can be detected, and allows inverting for all the independent elements of the elastic tensor. The method shown here at ambient pressure, can be applied up to moderately high pressures (about 20 GPa) as it ideally requires a sample with a perfectly smooth surface of about 50 to 100 $\mu$m diameter and a thickness of the order of tenths of microns.

Two examples are provided for experiments performed at high pressure and ambient temperature: (1) the determination of compressional sound velocities on polycrystalline Fe-2.2wt%C up to 15 GPa shown in Section 4 and (2) the determination of sound velocities of Ar in Section 5. Here, example (1) highlights the possibility to determine sound velocities on very thin (few $\mu$m) opaque samples. The arrival time of the longitudinal wave generated by the pump laser is directly measured. As the surface size of the sample is limited only by the size of the laser (2 $\mu$m diameter), the temporal mode can be exploited for echoes detection up to about 150 GPa. Combined with the knowledge of sample's thickness, obtainable for instance exploiting the equation of state, longitudinal sound velocity can be measured. The temporal mode in Brillouin detection shown in example (2) allows to determine the longitudinal sound velocity independently from the sample thickness, and can also be adopted up to very high pressures, but with the constrain of being limited to transparent samples.

Finally, picosecond acoustics measurements on a Mo foil laser heated up to 2400 K and compressed to 34 GPa in a diamond anvil cell are presented and discussed in Section 6. This example shows the first, to this date, picosecond acoustics experiment coupled to laser heating, and it is a proof of concept for the feasibility of experiments at extreme pressure and temperature conditions.

## 2 Picosecond acoustics

Among the techniques allowing the determination of sound velocities under high pressure, picosecond acoustics is one of the most versatile [34]. Picosecond acoustics covers a frequency range from ∼10 GHz to ∼700 GHz, thus bridging the gap between laboratory techniques such as ultrasonic interferometry [1] and Brillouin scattering [3] (from 1 MHz to 30 GHz) and inelastic neutron or X-ray scattering (from 1 to 10 THz) [34].

## 2.1 Operating principles

Picosecond acoustics is an optical pump-probe technique, where an ultrashort laser pulse is split into a pump and a probe beam and then focused on two opposite sides of the sample. In the setup at IMPMC, which is described here, the laser pulse has a duration of 100 fs with a tunable wavelength $\lambda$ in the 700 - 1000 nm range. The beams are focused down to spots on the sample of $\sim$2 $\mu$m diameter[2].

The pump beam is directly focused on the sample, if metallic, or on a transducer of complex refractive index $\tilde{n} = n + i\kappa$, where $n$ is the refractive index and $\kappa$ the extinction coefficient. The absorption of the pump beam generates a sudden temperature increase of few K over a thin portion of the sample corresponding to about one absorption length $\xi = \lambda/4\pi\kappa$ (for clarity, thermal diffusivity is neglected[3]). The corresponding thermal stress caused by thermal expansion relaxes by generating a strain field which propagates across the sample: i.e. the acoustic wave. The arrival of the generated acoustic wave at the opposite surface of the sample (or to the transducer) is detected by the probe beam, delayed in time with respect to the pump by means of a four meters long delay-line allowing to scan a temporal range of 13.34 ns with a minimum step size of 0.013 ps [13]. This temporal range fully covers the time between two subsequent pulses of the 80 MHz Mai Tai HP laser from Spectra-Physics (one pulse every $t_{laser}$=12.55 ns). The probe beam detects the arrival of the acoustic strain field at the opposite surface of the sample measuring the relative variation of the optical reflectivity, either in phase or intensity. Its variation can be expressed for an isotropic sample as [35]

$$\frac{\delta r(t)}{r_0} = 2ik_0 n_0 \left( \int_0^{+\infty} \eta(z,t)dz + \left(\frac{\partial \tilde{n}}{\partial \eta}\right) \frac{2\tilde{n}}{n_0^2 - \tilde{n}^2} \int_0^{+\infty} \eta(z,t) e^{2ik_0 \tilde{n} z} dz \right) \tag{1}$$

where $k_0$ is the laser wave vector and $n_0$ the refractive index of the material surrounding the sample (pressure transmitting medium or diamond anvil, depending on the type of loading), $\eta(z,t)$ the strain field within the sample and $u(t) = -\int_0^{+\infty} \eta(z,t)dz$ the surface displacement in the $z$ direction.

Following this equation, as the acoustic wave reaches the sample surface at the probe side, the optical reflectivity is altered in two ways: the photoelastic effect and the surface displacement. As shown by the decomposition of the reflectivity variation (Equation 1) in intensity (Equation 2a) and phase (Equation 2b) variations, the first modification contributes to the change of

[2]The irradiance delivered by the pump at the sample surface can be as large as $10^{14} - 10^{15} W/m^2$ (i.e. $10^4$ times the typical irradiance used in Raman experiments), but due to the femtosecond pulse width of the laser, the sample surface remains undamaged. Using ultrashort pulses prevent heat accumulation at the sample surface and hence prevent its degradation as long as the irradiance is kept well below the ablation threshold.

[3]The thermal length path $\gamma$ is $\sqrt{D\tau}$ where $\tau$ is the time width of the laser pulse and $D$ the thermal diffusivity of the target with $D = \kappa/\rho C_p$ ($\kappa$ the thermal conductivity, $\rho$ the density and $C_p$ the specific heat capacity). Classical $\gamma$ values are then around few nm for sample involved in this paper (e.g. $\gamma_{Al} = 2.7$ nm, $\gamma_{Fe} = 1.3$ nm and $\gamma_{Mo} = 2$ nm) well below their absorption lengths (@800 nm $\xi_{Al} = 8.5$ nm, $\xi_{Fe} = 19$ nm and $\xi_{Mo} = 19$ nm).

both the intensity and the phase of the reflectivity, whereas the second one only modifies the phase of the reflectivity signal.

$$\Re\left\{\frac{\delta r(t)}{r_0}\right\} = 2k_0 n_0\, \Im\left\{\left(\frac{\partial \tilde{n}}{\partial \eta}\right)\frac{2\tilde{n}}{n_0^2-\tilde{n}^2}\int_0^{+\infty}\eta(z,t)e^{2ik_0\tilde{n}z}dz\right\} \tag{2a}$$

$$\Im\left\{\frac{\delta r(t)}{r_0}\right\} = 2k_0 n_0\left(-u(t)+\Re\left\{\left(\frac{\partial \tilde{n}}{\partial \eta}\right)\frac{2\tilde{n}}{n_0^2-\tilde{n}^2}\int_0^{+\infty}\eta(z,t)e^{2ik_0\tilde{n}z}dz\right\}\right) \tag{2b}$$

Therefore, even when the intensity variation of sample reflectivity cannot be detected (i.e. the photoelastic effect is negligible), echoes can still be recorded using an interferometry system that detects the surface displacement.

The frequency domain characteristic of these experiments is obtained by the Fourier transform of the strain pulse propagating inside the sample $\eta(z,t)$ [35, 36] which is proportional to:

$$\frac{f}{f^2+(\frac{v_P}{2\pi\xi})^2},$$

where $v_P$ is the velocity of the created elastic wave and the maximum of the spectrum is given by $f_{peak} = v_P/2\pi\xi$. For example, using an aluminium transducer at 800 nm leads to $f_{peak} = 120$ GHz[4] and a frequency range from ∼20 to ∼700 GHz[5].

Essentially, picosecond acoustics detects the perturbations associated with the arrival of a wavefront at the sample surface. The arrival time is linked to the sample thickness and the energy velocity of this wavefront. The wavefront generated by the pump propagates within the sample with an energy velocity given by [38]

$$V_i = \frac{c_{ijkl}\, u_j u_l\, n_k}{\rho V_\Phi\, u_i^2} \tag{3}$$

where $\rho$ is the sample density, $c_{ijkl}$ the elastic tensor, $u_j$ and $n_k$ the vibration and propagation directions and $V_\Phi$ represents the phase velocity associated to this wavefront. This phase velocity being one of the 3 eigenvalues ($u_i$ the corresponding eigenvector) of the well-known Christoffel equation [38]

$$c_{ijkl}\; n_j n_k\, u_l = \rho\; V_\Phi^2\; u_i. \tag{4}$$

The energy velocity and the phase velocity in the general case are not equals and the experimental times must be derived from Equation 3 and not from the Christoffel equation. Exceptions are some special cases such as liquids, perfect polycrystalline samples or high symmetry directions in crystals (but not along the 3-fold axis).

[4]For Al $v_P$=6.47 km/s and at 800 nm $\xi$= 8.45 nm ($\kappa$ = 7.5226 [37]).

[5]The frequency range is calculated as $(m-\sqrt{m^2-1})f_{peak} < f < (m+\sqrt{m^2-1})f_{peak}$ where intensities $I(f)$ are higher than $I(f_{peak})/m$.

## 2.2 2D imaging mode

In the phonon imaging mode (one example of its application is shown in Section 3.2), the time-resolved reflectivity is recorded over an extended area of the sample surface at the probe side at different pump-probe delays (typically a region of 100x100 $\mu m^2$ is scanned). The resulting time-depending pattern is given by the intersection of the propagating acoustic wavefront with the sample surface at the probe side. This measurement mode is suitable for samples thicker than a few tens of micrometers, for which volume waves can propagate over a large $\varphi$ angle range, see Figure 1.

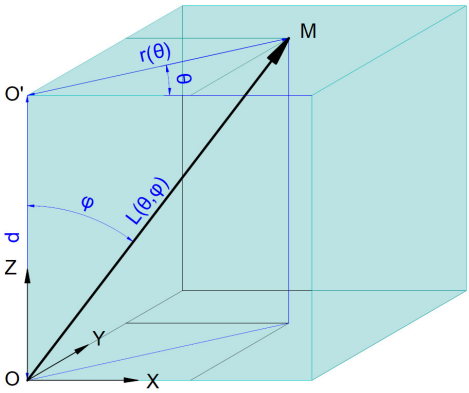


**Fig. 1**: At time $t = t_0$, the pump laser is focused in O. A wavefront is generated and propagates in all directions. At time $t = t_0 + \Delta t$, this wave crosses the sample surface at a generic M point (see experimental data in Figure 2). The problem is defined by the sample thickness $d$ and the energy velocity in the propagation direction $\overrightarrow{OM} = L(\theta, \varphi)\,\overrightarrow{n(\theta, \varphi)} = \sqrt{d^2 + r(\theta)^2}\,\overrightarrow{n(\theta, \varphi)}$

The acquisition of several images measured at increasing pump-probe time delay, the so-called "movie mode", allows to monitor the propagation of acoustic waves.

Patterns obtained in movie mode can be analyzed to derive the sample thickness and all the independent elements of the elastic tensor. Differently to the case of the temporal mode (see Section 2.3), when used in a high pressure run, no input on the sample compressibility (e.g. from literature data) is required.

Thanks to the recent software upgrade, recording an image over a 100x100 $\mu m^2$ area at the fastest speed and with 1 $\mu$m resolution takes only 12 seconds. A full movie with a $\lambda/3$ resolution and about 30 movie frames can now be obtained in roughly half an hour.

Figure 1 shows the pump axis as $z$, $O$ is the point where the pump laser is absorbed by the sample at the pump side at time $t_0$ and $O'$ the corresponding point along $z$ at the front sample surface. $\overline{OO'} = d$ is the sample thickness.

At time $t = t_0 + \Delta t$ the wavefront which propagates in direction $\overrightarrow{n(\theta,\varphi)}$ emerges at the front sample surface at point $M(d,\theta,\varphi,t)$, and $\overline{O'M} = r(\theta,t)$ is the distance of the energy wavefront from the pump axis in the direction $\theta$. Equation 5 can be easily derived

$$\Delta t = \frac{\|\overrightarrow{OM}\|}{\|\overrightarrow{V}\|} = \frac{\sqrt{d^2 + r(\theta,t)^2}}{V(\theta,\varphi)} \tag{5}$$

with $tan(\varphi) = r(\theta,t)/d$ and $V(\theta,\varphi)$ the solutions of Equation 3.

In our experimental setup, the measured arrival time $t$ is always $0 < t < 13.3$ ns. Accordingly, $\Delta t$ is experimentally known modulo the laser repetition rate $t_{laser}$: $\Delta t = \Delta t_{exp} + p\, t_{laser}$ where $\Delta t_{exp}$ is the observed value and $p$ an integer. This means that the waves detected by the probe are not necessarily generated by the same laser pulse. For example, on Figure 2, $p$=1 holds for the longitudinal wave while $p$=2 for the transverse wave.

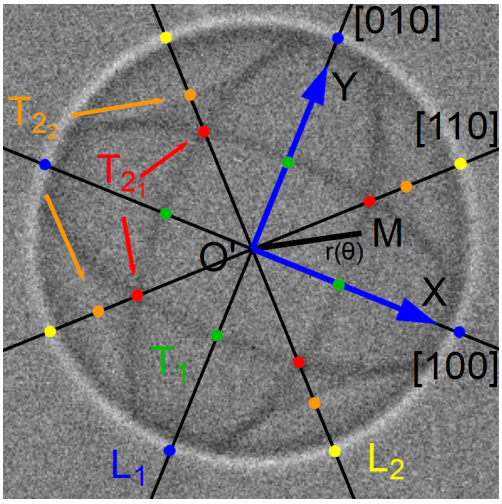


**Fig. 2**: Raw experimental data of a 100x100 $\mu$m$^2$ image obtained on a 190.5 $\mu$m thick Si sample with the pump-probe axis aligned along the [001] direction. The pseudo circular bright line is produced by the longitudinal wave. For polarization reasons, the complex dark line is produced by only one of the two transverse waves. On high symmetry directions, 5 points correspond to the longitudinal wave $L_1$ [100] (blue) and $L_2$ [110] (yellow) and to the transverse wave $T_1$ [100] (green) and $T_{2_1}$ (red) $T_{2_2}$ (orange) [110]. The gap between $T_{2_1}$ and $T_{2_2}$ is linked to the silicon anisotropy factor $\mathcal{A} = 2C_{44}/(C_{11}-C_{12}) = 1.563$.

The energy velocity $V(\theta,\varphi)$ is fitted to as many M experimental data points in form $M(t, r(\theta,t))$ as needed, through the adjustable parameters $d$ (the sample thickness) and the elastic tensor $c_{ijkl}$ for a known sample density $\rho$. It

should be noted that conversely to the thickness, the elastic tensor and the density cannot be independently adjusted and therefore the density cannot be obtained without an external hypothesis or a self-consistent addition to the fitting procedure.

Even for the simplest case of a cubic system (e.g. Si in Figure 2), Equation 3 does not have an analytical solution and the system must be numerically solved. The minimization process can be done either using a classical least square method ($\chi^2$ minimization) or a Reverse Monte-Carlo [39] with a test function $F_{test}$ as :

$$F_{test} = \frac{\sum_{i=1}^{N}(r_{exp}^2 - r_{cal}^2)}{N\sigma_{r_{exp}}^2} \tag{6}$$

with N being the number of data points extracted on the images obtained for different times for both longitudinal and transverse waves and $\sigma_{r_{exp}}$ being the uncertainty on the measurement of $r_{exp}$.

Compared to a classical $\chi^2$ minimization, the Reverse Monte-Carlo method is more robust and less sensitive to local minima. It does not depend on starting values and it should be chosen when the elastic tensor is poorly known or possesses a large number of independent elastic constants.

Using the fitting software it is possible to extract a complete set of elastic constants. In the case of Si, shown in Figure 2, the 3 independent elastic constants $C_{11} = 165.60(1)$ GPa, $C_{12} = 63.90(1)$ GPa and $C_{44} = 79.50(1)$ GPa are obtained with a good accuracy.

These values are very close to those determined using classical ultrasound method (respectively 165.78(10), 63.93(13) and 79.62(5) GPa)[40–42] and show that our uncertainty is better than 0.1%.

The same software can be used for simulation purposes on any sample whatever its symmetry and orientation and can generate high resolution images ($\Delta\theta = 8 \cdot 10^{-3}$ rad and $\Delta\varphi = 3.5 \cdot 10^{-5}$ rad) at 10 frames/s speed.

The precision and the accuracy of picosecond acoustics measurements formally depend on the laser characteristics, such as the uncertainty on the value of the laser repetition rate and on the wavelength. However, current technology is such that the uncertainty on these parameters is negligible. The accuracy of 2D imaging operating mode mostly depends on the accuracy of the density determination. On the other hand, the absorption length of the laser is the main aspect influencing the precision, as it directly affects the width of the acoustic signal at the probe side of the surface, and consequently the scatter in the determination of the value of $\|\overrightarrow{OM}\|$. A perfect orientation of the single crystal in the expected direction is crucial for the accuracy of the results, while random defects in the single crystal mostly influence the precision of the measurement.

## 2.3 Temporal mode

When 2D surface scanning is not possible, for example for thin samples (few $\mu$m thick) or when fast measurements are required, data acquisition in temporal

mode is a suitable alternative. Notably this is proven to be a valuable way to detect in situ phase transitions [7, 12–15]. Moreover, when both pump and probe beams are collinear, $\varphi$ is always zero and, for single-crystals oriented along a high symmetry direction (but 3-fold axis), the energy and the phase velocities are equals. In liquids or polycrystals the wavefronts are spherical and energy and phase velocities are equals. Then, in this mode, most of the time, the Christoffel equation (Equation 4) can be used to extract the elastic constants from experimental data as typically done in the classical pulse-echo method used in ultrasonic set-up [43].

### 2.3.1 Echoes detection

In its most basic configuration, with collinear pump and probe (pump in O and probe in O' in Figure 1) focused at the two opposite surfaces of an opaque sample, as shown in Sections 4 and 6, or for a double-coated sample, as shown in Section 3.2, the sound velocity $v$ can be obtained through:

$$v = \frac{d}{\Delta t} = \frac{d}{t_1 - t_0} \tag{7}$$

where $d$ is the thickness of the sample, $t_0$ is the time of pump and probe optical pulse coincidence and $t_1$ is the arrival time of the first acoustic echo at the probe side of the sample. In a high pressure experiment the thickness variation has to be derived by some other optical or mechanical *in-situ* measurement or by a predetermined EOS. Nevertheless, due to their sensitivity, these measurements are always well adapted for the qualitative analysis sufficient for phase diagram determination even when $d$ and its variation are unknown.

In this operation mode the precision of the measurement depends on, once again, the absorption length, but the uncertainty on the velocity both in terms of precision and accuracy is mostly affected by the determination of the sample's thickness and $t_0$. A careful and precise determination of the sample thickness and the time of pump and probe coincidence is thus crucial for a correct determination of the compressional sound velocity in echoes detection operation mode.

### 2.3.2 Brillouin detection

For transparent samples, the acoustic wave is generated by focusing the pump on a transducer coated on the pump side of the sample (as in [8] and in the examples shown in Section 3.1 and 5). The probe is focused through the sample on the other side of the transducer. The interference between the probe light reflected by the acoustic wavefronts, which can be seen as a density wave propagating at the sound velocity, yields oscillations. As this signal is tightly related to the Brillouin effect, oscillations are referred to as Brillouin oscillations (Figure 3).

During their propagation in the sample, these Brillouin oscillations are attenuated. The frequency $f$ of the Brillouin signal is then obtained through

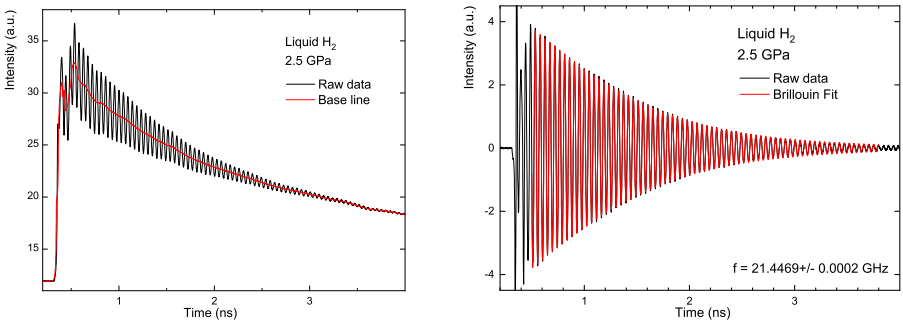


**Fig. 3**: Brillouin oscillation collected on liquid $H_2$ sample in a diamond anvil cell [8]. Relative accuracy on the frequency is on the order of $10^{-5}$. In the left panel is shown the raw reflectivity data obtained from a DAC loaded sample and base line used for Brillouin signal extraction. In the right panel are represented the extracted and fitted Brillouin oscillations.

a fit to a sinusoidal function damped by an exponential:

$$y = A \cdot \sin[2\pi f(t - t_0) + \phi] \cdot \exp^{-B(t-t_0)}, \tag{8}$$

where $\phi$ is the phase of the sinusoidal signal, $A$ indicates the amplitude of the signal and $t_0$ the origin of the Brillouin generation time. In this scheme, due to conservation rules, only longitudinal acoustic phonons can be detected and their experimental frequency $f$ depends on the sound velocity $v$, the refractive index $n_0$ of the material and the wavelength of the probe laser $\lambda$:

$$v = \frac{f\lambda}{2n_0}. \tag{9}$$

The acoustic attenuation $\alpha_0$ can be obtained from the $B$ coefficient of Equation 8 as:

$$\alpha_0 = \frac{2n_0 B}{\lambda f^3} \tag{10}$$

where we have assumed the classical hypothesis $\alpha = \alpha_0 f^2$.

It should be noted that in order to extract the absolute value of the acoustic attenuation $\alpha_0$, the exponential part of the signal has to be multiplied by a transfer function that takes into account optical properties of the setup (more details can be found in [14]).

For an absolute determination of the sound velocity at high pressure, the refractive index variation has to be known or modeled. Nevertheless, due to their sensitivity, these measurements can be used either to obtain a 3D image of the sample [6], or to get the values of the sound velocity at their extremes by frequency dispersion studies [8], even if the $n_0$ variation is unknown.

The precise measurement of the Brillouin signal is mostly dominated by the quality of the single- or poly-crystal. Both the accuracy and the precision of the resulting compressional velocity are also strongly affected by the uncertainties on the material's refractive index.

# 3 Elastic properties of single-crystal MgO at ambient conditions

MgO is an important constituent of the Earth's lower mantle, as a component of ferropericlase (Mg,Fe)O [25, 44–47], and an archetypal end-member used for planetary modelling. With its elastic properties being fairly well known [48, 49], MgO is an excellent case study to test the newly upgraded experimental setup.

Temporal, imaging and movie-mode measurements have been performed at $\lambda$= 800 nm on a commercially available (Optowise) single-crystal of MgO oriented along the [001] direction[6], with a surface of 2x2 mm$^2$ and a nominal thickness of 100(20) $\mu$m. MgO is transparent at this wavelength, as such it needs to be coated at the pump side to allow the absorption of the laser and to generate an acoustic wave. Two different sets of measurements have been performed on two differently coated samples. The first sample was coated on only one side with an Al layer $\sim$ 650 nm thick by physical vapour deposition (PVD) machine at IMPMC. The second sample was coated on both sides with Al using an evaporation deposition machine at INSP[7]. In this second case, the Al transducers had a thickness of 200 nm and 100 nm at the pump and probe side, respectively.

## 3.1 Determination of $v_{L<100>}$ on a single coated sample

The Brillouin signal of MgO was measured in the configuration shown in the left panel of Figure 4. MgO has a cubic symmetry (space group Fm$\bar{3}$m) and for this measurement the <100> direction was oriented parallel to the pump-probe axis. The Brillouin oscillations are shown in the right panel of Figure 4: the raw measured signal is shown in black, the Brillouin signal obtained after extracting the signal baseline (purple) in blue.

Besides the Brillouin oscillation, the raw signal also presents sharp echoes as pointed out in Figure 4. These are the outcome of multiple reflections of the acoustic signal propagating in the $\sim$650 nm thick Al transducer. 650 nm thickness is in fact about 10 times the optimal deposition thickness required for a good strain field generation in an Al transducer. The presence of these echoes can be exploited to determine the time $t_0$ of generation of the acoustic signal at the Al - air interface. Time $t_0$ is calculated as:

$$t_0 = t_1 - \frac{t_3 - t_1}{2} \tag{11}$$

[6]Note that from here on, the angle brackets indicate all the equivalent directions, while the square brackets a well defined direction. <100> thus includes all the 6 equivalent directions [100], [0$\bar{1}$0], [001], [$\bar{1}$00], [0$\bar{1}$0] and [00$\bar{1}$].

[7]Institut des NanoSciences de Paris, Sorbonne Université, CNRS UMR 7588, Paris (France)

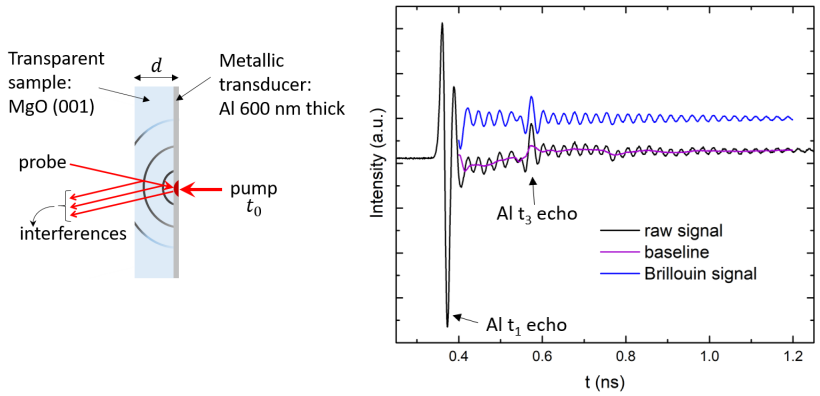


**Fig. 4**: Brillouin signal on a single-crystal MgO with the <100> direction parallel to the pump-probe axes. Left panel shows the measurement scheme: pump and probe lasers are focused at the two opposite sides of the Al deposition, at the Al - air and Al - MgO interface respectively. The interference between the probe laser and the acoustic wave propagating in the MgO sample gives rise to the Brillouin oscillations visible in the right panel. Note that the probe laser and its reflections are perpendicular to the deposition, they are shown with an angle to better represent the origin of the Brillouin oscillations. In the right panel, the raw data is represented in black, the signal baseline in purple and the Brillouin signal in blue.

where $t_1$ is the first arrival of the acoustic wave at the Al - MgO interface, and $t_3$ is the echo after subsequent reflections at the Al - MgO and Al - air interface. In the signal shown in the right panel of Figure 4, $t_1 = 0.3721(1)$ ns and $t_3 = 0.5738(1)$ ns were obtained by fitting the central position of the echoes with a Lorentzian function, resulting in $t_0 = 0.2713(2)$ ns.

A fit of the extracted Brillouin signal in the 0.42 - 1.12 ns range using Equation 8 is shown in the left panel of Figure 5. The fitted parameters are the frequency $f = 39.25$ GHz, the amplitude $A = 4.45\ 10^{-5}$, the phase $\phi =$ -1.86 rad and the constant $B = 8.90\ 10^{-8}$ s$^{-1}$ while $t_0$ was fixed to the previously calculated value of 0.2713 ns.

Using the known refractive index for MgO at $\lambda$= 800 nm ($n_0 = 1.7276$ [50]), we finally derive $\alpha_0 = 1.7\ 10^{-16}$ m$^{-1}$ Hz$^{-2}$, value obtained without considering the transfer function correction (see Section 2.3.2).

The resulting sound velocity of $v_{L<100>} = 9060$ m/s is possibly affected by the presence, within the considered temporal range, of the $t_3$ echo around 0.57 ns. In order to avoid this perturbation to the Brillouin oscillation, we have performed independent fits in 4 different ranges, as indicated in the right panel of Figure 5. The value of the longitudinal acoustic wave velocity along the [001] direction was then computed as the average of the velocity values obtained in

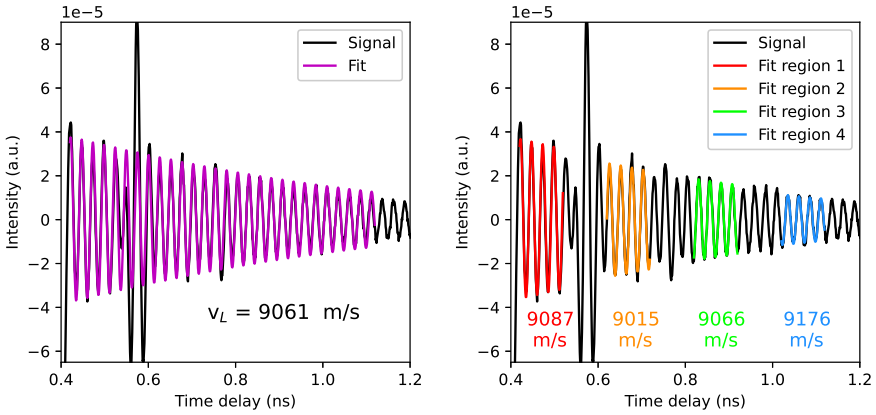


**Fig. 5**: Fit of the Brillouin signal obtained in the [001] direction. In the left panel, the fit of the Brillouin signal to Equation 8 results in a longitudinal velocity of $V_{L<100>} = 9061$ m/s. This fit is perturbed by the presence of the acoustic echoes. In the right panel, the fit is performed on four different color-coded ranges. The velocity obtained for each range is reported accordingly to the color code. The resulting average velocity is $v_{L<100>} = 9090(60)$ m/s with the uncertainty corresponding to one standard deviation.

the four selected time ranges, assuming as uncertainty the standard deviation. The resulting value is $v_{L<100>} = 9090(60)$ m/s [8].

In a cubic system, the longitudinal velocity along <100> depends on the elastic constant ($C_{11}$) and the density $\rho$ according to:

$$v_{L<100>} = \sqrt{\frac{C_{11}}{\rho}}, \tag{12}$$

Once taking $\rho = 3.584(4)$ g/cm$^3$ as value of the density of MgO at ambient conditions[48, 49] we get $C_{11} = 296.1(40)$ GPa, in agreement with literature values of 297.7(30) GPa [48] and 297.0(1) GPa [51].

## 3.2 Determination of the elastic tensor on a double coated MgO sample

Schematics of measurements on samples in the double coated configuration is presented in the left panel of Figure 6, where, differently to the case presented in Section 3.1, the probe laser is focused on the Al coating at the probe side of the sample. In this configuration it is possible to image, for each chosen pump-probe time delay, the intersection of the acoustic wave with the surface of the

[8] The same value $v_{L<100>} = 9090(63)$ m/s is obtained using the sliding sinusoidal fit shown in Section 5 in the range 0.6 - 1.5 ns. The obtained velocity is randomly scattered around the average value, showing good homogeneity of the MgO single-crystal.

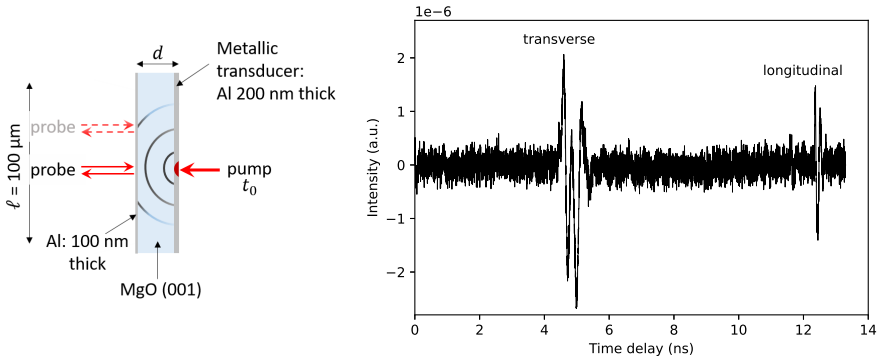


**Fig. 6**: The measurement scheme for double coated MgO is represented in the left panel: the pump laser is focused at the right side of the sample, on a 200 nm thick Al transducer, the probe laser is focused at the left side of the sample on a 100 nm thick Al layer. The red solid arrows indicate the configuration where the probe is in coincidence with the pump. In imaging mode the probe is scanned over a region of the sample surface of $\ell \times \ell = 100{\times}100\ \mu\text{m}^2$, as indicated by the dashed red arrows. The right panel shows the signal in temporal mode obtained when the probe is in coincidence with the pump. The arrival time of the longitudinal wave is at $t_L = 12.398$ ns. The signal at 4.659 ns is possibly misleading, as this corresponds to a transverse wave crossing the point of coincidence of pump and probe, but whose first arrival, as can be seen in Figure 7, happens prior to this time, but cannot be detected since out of the pump-probe axis.

sample. The right panel of Figure 6 shows a temporal signal obtained when the pump and the probe lasers on the same axis. Exploting the $t_0$ and longitudinal velocity in the [001] direction obtained in the previous section, and the arrival time of the longitudinal wave here detected as $t_L = 12.398$ ns, it is possible to calculate with precision the thickness $d$ of the sample using Equation 7:

$$d = v_{L[001]} \cdot (t_1 - t_0) = 110.2(7)\ \mu m, \tag{13}$$

which is compatible with the nominal thickness of 100(20) $\mu$m.

In imaging mode, the intersection of the acoustic waves with the probe side of the sample is investigated, as it is shown in Figure 7 for the transverse (shown at the top) and the longitudinal wave (shown at the bottom). The symmetry of the transverse wave helps detecting the orientation of the crystal, as illustrated in the top right image of Figure 7.

Figure 7 shows the propagation of the transverse wave, similarly to the example of Si reported in Figure 2. The first detection of the transverse wave is out of the pump-probe axis. Moreover, the $T_{2_1}$-$T_{2_2}$ splitting (see Figure 2) is approximately of the same order of magnitude. This is a strong indication that the anisotropy factor $\mathcal{A} = 2C_{44}/(C_{11} - C_{12})$ of MgO is comparable to

the one reported for Si in Section 2.2. Note that in the top of Figure 7 two transverse waves were modeled (shown in red). However, the transverse wave having its polarization parallel to the surface plane cannot be detected.

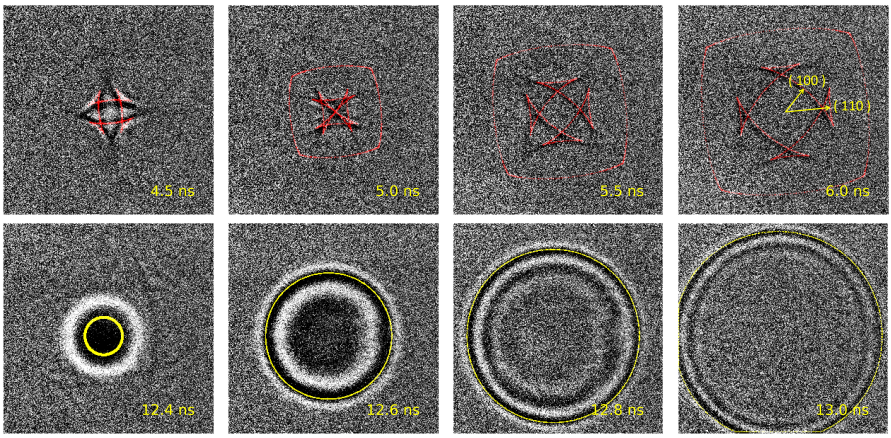


**Fig. 7**: The measured acoustic wave propagating in MgO is reported in the four top images superposed to the simulated transverse wave (simulation in red). Similarly, in the bottom images for the longitudinal (simulation in yellow) waves. At the bottom-right of each image is reported the pump-probe time delay.

The orientation of the MgO cyrstal was determined using the recently developed software that allows superimposing measurements and simulations. The propagation of the acoustic waves over pump-probe time delay along the crystallographic directions <100> and <110> is represented in Figure 8.

The distance from the pump-probe axis of the transverse and longitudinal waves ($\overrightarrow{O'M}$ in Figure 1) at the sample surface for the <100> and <110> directions for each recorded image at a known delay time, is the input data to the software described in Section 2.2. The control parameters are the set-up values, such as $t_0$, the laser repetition rate $t_{laser}$=12.55 ns, the sample symmetry and orientation, as well as its density $\rho$, while the adjustable parameters are the $c_{ijkl}$ and the sample thickness.

Initial and refined values are summarized in Table 1, where they are also compared to the literature data. As expected from the raw transverse images, the anisotropy factor data obtained for MgO ($\mathcal{A} = 1.561$) is very similar to the one of silicon ($\mathcal{A} = 1.563$).

Our results are in very good agreement with those obtained using Brillouin spectroscopy [48, 51]. The reported uncertainties arise from the $\chi^2$ minimization software and depend both on the number of data points (109 in this case) and their accuracy (less than 0.5 $\mu m$). They were multiplied by a factor 2 in order to take into account neglected systematic errors and/or algorithm bias.

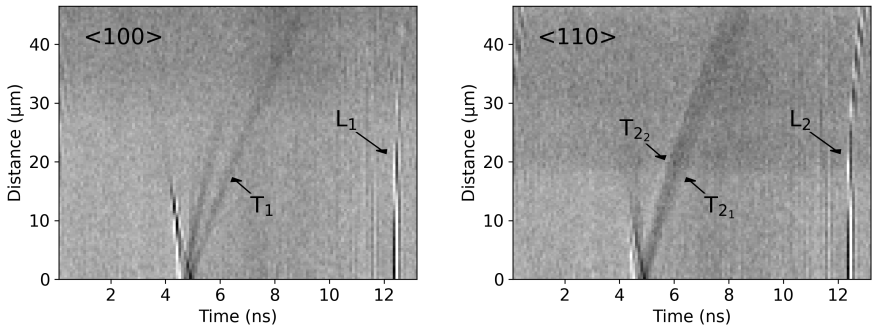


**Fig. 8**: Radial integration of the images shown in Figure 7 for the directions <100> and <110>. The propagation of the transverse and longitudinal acoustic waves is evidenced. Due to their polarization, only one transverse wave is detected. On the 2 images, this transverse wave appears first out of the pump-probe axis. This effect, known as self focusing phonon, depends on the anisotropy factor $\mathcal{A} = 2C_{44}/(C_{11} - C_{12})$.

**Table 1**: Parameters initially guessed for the inversion program and refined results for the sample thickness $d$ and the three independent elements of the elastic tensor $C_{11}$, $C_{12}$ and $C_{44}$ of cubic systems. The density marked with an asterisk (*) is from Ref. [48]

| | Guessed | **Refined (this work)** | Sinogeikin 2000 [48] | Zha 2000 [51] |
|---|---|---|---|---|
| $\rho$ (g/cm$^3$) | 3.584* | - | 3.584 | 3.585 |
| $d$ ($\mu$m) | 110.2 | **110.2(2)** | - | - |
| $C_{11}$ (GPa) | 300. | **297.0(2)** | 297.7(10) | 297.0(1) |
| $C_{12}$ (GPa) | 100. | **95.5(5)** | 95.3(10) | 95.2(7) |
| $C_{44}$ (GPa) | 160. | **157.3(3)** | 154.5(15) | 155.7(5) |

The uncertainties found here are of the same order of magnitude of those reported by Zha et al.[51]. We can therefore conclude that picosecond 2D imaging mode and Brillouin spectroscopy provide comparable results. One of the main advantages of picosecond acoustics lies in the much shorter collection time, of the order of one hour for the presented measurement versus several hours to several days for a classic Brillouin technique. Sound velocities can also be extracted from inelastic x-rays or neutron scattering data obtained on large facilities set-ups but experiments are known to be very time consuming and only few runs, first approved by a local commissioning, are planned each year. Finally, we want to emphasize that differently from the classical ultrasonic techniques, where the travel time has to be measured on different samples for each crystallographic orientation [52], with picosecond acoustics a single experiment on one crystallographic orientation allows to obtain the complete elastic tensor at once.

The apparent disagreement between the $C_{11} = 296.1$ GPa obtained through Brillouin oscillations and the 2D imaging mode ($C_{11} = 297.0$ GPa) could be due to the assumed value for the MgO refractive index, taken from the literature, and imposed during the Brillouin calculation. Using the value of $C_{11}$ obtained with the 2D imaging mode to recalculate the refractive index of MgO at ambient conditions, we obtain $n_0 = 1.725$ close to 1.7276 used in our calculations.

The obtained value of the thickness and the elastic constants have been used to simulate the propagation of longitudinal and transverse waves for an MgO sample oriented to [001]. The simulation is shown in Figure 7 superimposed on the experimental images, in red and yellow for the transverse and longitudinal waves respectively. The good agreement between the experiment and simulation is a good indication of the accuracy of the parameters obtained with the inversion analysis.

Given the cubic symmetry of the system, the Voigt and Reuss bulk[9] (K) and shear[10] (G) moduli were calculated as follows:

$$K_{Voigt} = \frac{C_{11} + 2C_{12}}{3} = 162.7 \text{ GPa} \tag{14a}$$

$$G_{Voigt} = \frac{C_{11} - C_{12} + 3C_{44}}{5} = 134.7 \text{ GPa} \tag{14b}$$

$$K_{Reuss} = \frac{1}{3(S_{11} + 2S_{12})} = 162.7 \text{ GPa} \tag{14c}$$

$$G_{Reuss} = \frac{5}{4S_{11} - 4S_{12} + 3S_{44}} = 128.4 \text{ GPa} \tag{14d}$$

where the compliance constants were obtained by inverting the elastic tensor ($S_{ij} = C_{ij}^{-1}$ [53]). The longitudinal and shear acoustic velocities $v_P$ and $v_S$ can then be calculated following the Adams-Williamson equations:

$$v_P = \sqrt{\frac{K + 4G/3}{\rho}} \tag{15a}$$

$$v_S = \sqrt{\frac{G}{\rho}} \tag{15b}$$

where $\rho$ is the sample density.

The resulting velocities are summarized in Table 2, where the values are calculated by averaging the results obtained by perturbing the initially guessed values of the elastic constants, and the uncertainty is the standard deviation of the obtained values.

The wave velocities obtained in this study and in literature data are in agreement within the uncertainties, proving that picosecond acoustics is a

[9] In cubic crystals, $(S_{11} + 2S_{12}) = (C_{11} + 2C_{12})^{-1}$, $K_{Reuss}$ and $K_{Voigt}$ are always equals.

[10] In cubic crystals $G_{Voigt} = (2C' + 3C44)/5$ and $1/G_{Reuss} = (2/C' + 3/C44)/5$ with $C' = (C_{11} - C_{12})/2$, their difference depends only on the anisotropy factor $\mathcal{A}$ and $G_{Reuss} < G_{Voigt}$.

**Table 2**: Compressional and shear velocities calculated using bulk and shear moduli obtained from Voigt, Reuss, from the average between the Voigt and Reuss. These results are compared to the literature.

| | Voigt this work | Reuss this work | Average this work | Kono 2010 [49] | Sinogeikin 2000 [48] | Zha 2000 [51] |
|---|---|---|---|---|---|---|
| $v_P$ (km/s) | 9.74(2) | 9.63(2) | 9.68(2) | 9.665(7) | 9.69(5) | 9.68(4) |
| $v_S$ (km/s) | 6.10(2) | 5.97(2) | 6.04(2) | 5.987(4) | 6.03(3) | 6.06(3) |

reliable, and to many extents faster and more versatile alternative to other laboratory techniques [48, 49, 51] for determining the elastic constants.

# 4 Compressional sound velocity of Fe-2.2wt%C at high pressure

Picosecond acoustic measurements have been performed on a Fe-C polycrystalline foil at high pressure in a diamond anvil cell up to 15 GPa using Ar as pressure transmitting medium. The sample was deposited by DEPHIS[11] on a 1 mm thick glass slide with a nominal composition of Fe - 1.4wt% C. The composition was measured to be Fe - 2.2(1)wt% C with the Cameca SX100 electron microprobe at CAMPARIS, Sorbonne Université. The sample thickness was determined at IMPMC using profilometry and by visual observation of the sample section with the scanning electron microscope (SEM). The thickness resulting from the average of the two techniques is $d = 2.20(5)$ $\mu$m.

## 4.1 Measurements at ambient conditions

Prior to loading the sample inside the DAC, an acoustic measurement was performed on Fe-C at ambient conditions, with the Mai Tai laser wavelength operating at $\lambda = 960$ $\mu$m, value more suited for high temperature measurements (see Section 6). Differently from the experiment on MgO described in Section 3.1, the laser pump at this wavelength is directly absorbed by the metallic sample and no additional transducer is required. The measurement configuration is shown in the left panel of Figure 9, where the pump is focused at the sample - glass interface and the probe is focused at the opposite side of the sample. The right panel of Figure 9 shows the resulting time domain picosecond acoustics measurement, where three sharp acoustic echoes are visible. They arise from multiple reflections of the acoustic wave at the sample - air and sample - glass interfaces at $t_1 = 0.703$ ns, $t_3 = 1.467$ ns and $t_5 = 2.229$ ns. Detection of multiple echoes allows to determine the pump-probe coincidence $t_0 = 0.320$ ns.

[11] DEpôts PHysiques InnovantS, 25460 Etupes France

The obtained sound velocity of the alloy, independent from $t_0$, is:

$$v_P = \frac{d}{(t_3 - t_1)/2} = 5.76(14)\text{km/s}. \tag{16}$$

Note that in this case the sample is a polycrystal, hence, under the assumption of random and homogeneous grain distribution in the sample, the obtained sound velocity is the average longitudinal velocity along all crystallographic directions.

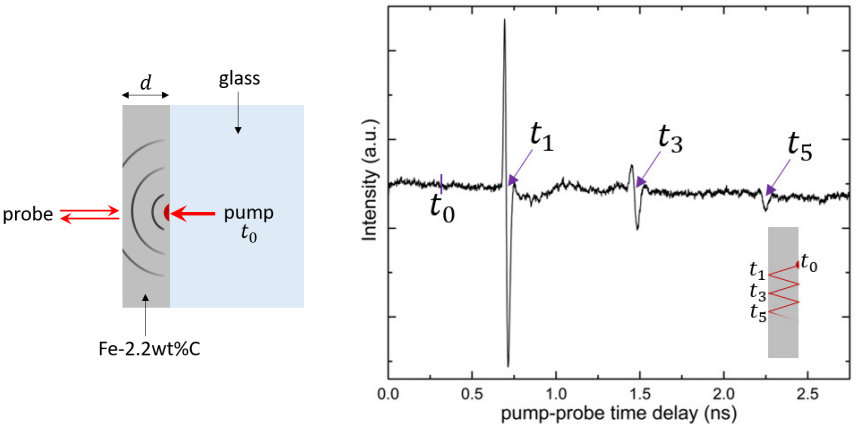


**Fig. 9**: Measurement configuration for the Fe-2.2wt%C sample (left panel) and time domain picosecond acoustic measurement (right panel), where the acoustic echoes $t_1$, $t_3$ and $t_5$ are indicated by purple arrows. The $t_3$ and $t_5$ echoes are generated by multiple reflections inside the sample, as represented in the bottom right part of the graph. Note that this representation is helpful to visualize the appearance of the echoes, but it does not correspond to reality, as the three echoes are detected in the same position of the sample.

## 4.2 High pressure measurements

High pressure conditions were generated using a membrane-driven DAC equipped with single-crystal diamonds, having a culet diameter of 400 $\mu$m. A 200 $\mu$m thick rhenium gasket, pre-indented to a thickness of 45 $\mu$m, was laser drilled in the center of the pre-indentation to make a hole of 200 $\mu$ serving as sample chamber. The sample was removed from the glass slide support, cut to dimensions of $50 \times 50$ $\mu$m$^2$ and positioned on the diamond culet together with a ruby sphere ($Cr:Al_2O_3$) acting as pressure gauge. The sample chamber was filled with Ar gas as pressure transmitting medium (PTM), which maintains quasi-hydrostatic conditions up to 15-20 GPa [54]. A schematic representation for the high pressure measurements is shown in the left panel of

Figure 10, where the pump and probe lasers are focused on the two sides of the Fe-C sample, with the diamonds and the pressure transmitting medium being transparent to the laser at $\lambda = 960$ nm. The acoustic wave generated at the pump side of the sample propagates through the Fe-C alloy and is then transmitted to the Ar pressure transmitting medium. The obtained time domain signal thus contains the arrival time of the acoustic wave at the probe side of the Fe-C and the Brillouin signal from the pressure transmitting medium. The Brillouin Ar signal as a function of pressure is discussed in Section 5.

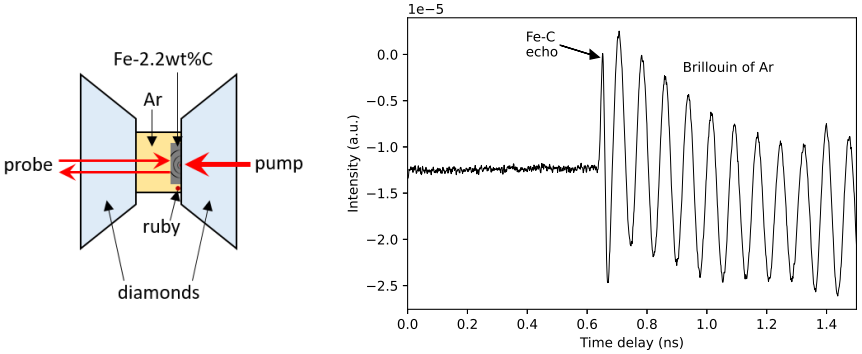


**Fig. 10**: Left panel: scheme for picosecond acoustic measurements of Fe-C at high pressure in the diamond anvil cell. Right panel: Time domain picosecond acoustic measurement at 6.68(7) GPa. The arrival time $t_1$ of the acoustic wave at the probe side of the sample is indicated as Fe-C echo. The acoustic wave is transmitted to the PTM, resulting in the Brillouin oscillations from Ar.

The arrival time of the acoustic wave for Fe-C was measured as a function of pressure up to around 15 GPa. Table 3 reports all pressure points collected in compression, from ambient to 14.6(1) GPa, and then in decompression to ambient pressure. The pressure was left to stabilize for about 20 minutes before performing the picosecond acoustics measurements, leading to a very small uncertainty in the pressure, calculated from the difference in the ruby fluorescence before and after each acoustic measurement.

In the high pressure configuration, the laser passes through the diamonds and, due to the modified optical path, the reference time $t_0$ for the pump arrival is slightly different than in the configuration presented in Section 4.1. To recalculate $t_0$ we thus measured a time domain picosecond acoustics signal of the sample inside the DAC after decompression. With the assumption that $t_0$ is not influenced by the compression of the diamonds and by the presence of Ar as PTM, we obtained $t_0 = 0.308(4)$ ns, from the measured $t_1 = 0.676(2)$

ns and $t_2 = 1.412(2)$ ns. As expected[12], this value is smaller than the one calculated in Section 4.1.

**Table 3**: Arrival times of the acoustic wave as a function of pressure. In the first column 'c' indicates data obtained in compression and 'd' those in decompression. Reported thickness are calculated for pure Fe and $Fe_3C$ samples considering an initial thickness of 2.12 $\mu$m according to the EOS of [55] and [56] respectively. These values are used to determine the thickness of Fe-2.2wt%C as linear mixing of the two end members. The thickness of Fe-2.2wt%C is then used to calculate the velocity $v_P$. The uncertainties are 2 ps on the arrival time, 0.05 $\mu$m on the thickness and 0.14 km/s on the velocity. Except for the point indicated with (*) where $t_0 = 0.320(4)$ ns, for all the other points $t_0 = 0.308(4)$ ns.

| | P (GPa) | $t_1$ (ns) | $d_{Fe}$ ($\mu$m) | $d_{Fe_3C}$ ($\mu$m) | $d_{Fe-2.2wt\%C}$ ($\mu$m) | $v_P$ (km/s) |
|---|---|---|---|---|---|---|
| | amb* | 0.703 | - | - | 2.20 | 5.76 |
| c | 1.6(7) | 0.672 | 2.113 | 2.114 | 2.113 | 5.81 |
| c | 3.3(1) | 0.662 | 2.106 | 2.107 | 2.106 | 5.95 |
| c | 4.5(1) | 0.659 | 2.101 | 2.103 | 2.101 | 5.99 |
| c | 6.7(1) | 0.652 | 2.093 | 2.096 | 2.093 | 6.08 |
| c | 8.8(9) | 0.643 | 2.085 | 2.089 | 2.085 | 6.22 |
| c | 10.7(1) | 0.637 | 2.078 | 2.083 | 2.079 | 6.32 |
| c | 11.7(6) | 0.635 | 2.075 | 2.080 | 2.075 | 6.35 |
| c | 13.4(3) | 0.632 | 2.069 | 2.075 | 2.070 | 6.39 |
| c | 14.6(1) | 0.625 | 2.065 | 2.071 | 2.066 | 6.52 |
| d | 13.9(1) | 0.626 | 2.067 | 2.073 | 2.068 | 6.50 |
| d | 11.2(1) | 0.633 | 2.076 | 2.081 | 2.077 | 6.39 |
| d | 10.3(1) | 0.634 | 2.080 | 2.084 | 2.080 | 6.38 |
| d | 0.7(1) | 0.674 | 2.117 | 2.117 | 2.117 | 5.78 |
| d | amb | 0.676 | 2.120 | 2.120 | 2.120 | 5.76 |

The arrival times $t_1$ measured at high pressure are reported in Table 3. The data collected in compression and in decompression are consistent starting from 1.6(7) GPa, whereas the measurements in air before and after compression are different. This suggests that the sample is plastically deformed at the first stage of compression, but that no further significant plastic deformation occurs over the investigated pressure range. For this reason, in the estimation of the sample thickness at high pressure, which relies on an EOS, we consider for $d_0$ (the reference value at ambient conditions) the value of the thickness obtained from travel time measurements on the recovered sample, i.e. the last point in Table 3. Using the compressional sound velocity $v_P(0) = 5.76(14)$ km/s obtained on the sample on the glass slide at ambient conditions we can derive $d_0 = v_P(0) * (t_1 - t_0) = 2.12(5)$ $\mu$m.

[12]In the ambient conditions configuration only the pump has to go through 1 mm of glass, while in the high pressure configuration both the pump and the probe go through two equivalent diamonds.

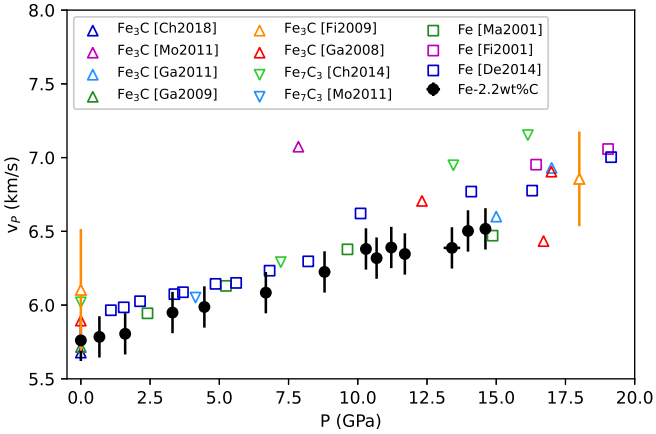


**Fig. 11**: Compressional sound velocities for Fe-2.2wt%C measured in this work by picosecond acoustics and compared to literature data for Fe (Ma2001 [57], Fi2001 [58] and De2014 [7]), $Fe_3C$ (Ch2018 [59], Mo2011 [60], Ga2011 [61], Ga2009 [62], Fi2009 [63], Ga2008 [56]) and $Fe_7C_3$ (Ch2014 [64], Mo2011 [65]).

In Table 3, the reported variation of thickness of the Fe-C alloy is obtained by considering a linear mixing between the EOS of pure iron [55] and $Fe_3C$ [56]. We stress, however, that the estimated thicknesses only marginally depend on this approximation, as thicknesses estimated assuming either end-member EOS are very close (see Table 3). The resulting velocities as a function of pressure are reported in Table 3 and shown in Figure 11, where they are compared to the literature for pure Fe, $Fe_3C$ and $Fe_7C_3$. Once compared to accurate velocity determination in pure Fe [7], our C-bearing alloy shows velocities systematically lower. This is different to what reported for Fe-Si alloys [10], where inclusion of Si increases $v_P$ with respect to pure Fe, and can be explained by the different incorporation mechanisms, substitutional in the case of Si and interstitial in the case of C [66]. Literature measurements on stoichiometric $Fe_3C$ or $Fe_7C_3$ are more scattered. Within the uncertainties, and over the pressure range investigated here, the presence of carbon does not seem to affect the pressure-derivative of the compressional sound velocity.

From a methodological point of view, we note that the data set presented here was collected in a total of about 10 hours, including the waiting time for stabilizing the pressure. For each pressure point, the time domain picosecond acoustic measurement signal was collected in 2.5 minutes. In this regard, picosecond acoustics offers a significant advantage with respect to synchrotron techniques such as inelastic X-ray scattering.

# 5 Ar: a randomly-oriented transparent crystal at high pressure

The sound velocity of Ar as a function of pressure was determined using the same setup employed for measurements on the Fe-C metallic alloy (left panel of Figure 10). The Fe-C foil acts as a transducer where the acoustic signal is generated and transmitted to the Ar inside the sample chamber. At pressures higher than 1.3 GPa [67] Ar becomes solid and crystallizes in the fcc structure. Once compression is not *ad hoc* controlled, it is not possible to know *a priori* if Ar crystallized as a polycrystal or as a single-crystal and how it is oriented.

Brillouin signals of Ar were measured in the pressure range between 1.6(7) and 14.6(1) GPa. An example of a Brillouin signal of Ar at 14.6 GPa in the time delay range between 0.75 - 2.00 ns is shown on the left panel of Figure 12. The sudden increase in the amplitude of the oscillations visible around 1.3 and 1.8 ns relates to the $t_3$ and $t_5$ echoes in the Fe-C sample (see Section 4.2). The accurate determination of the arrival of these echoes is, however, prevented by the Ar Brillouin oscillation. At the same time, presence of echoes complicate the analysis of the Brillouin oscillations in the time windows near their arrival.

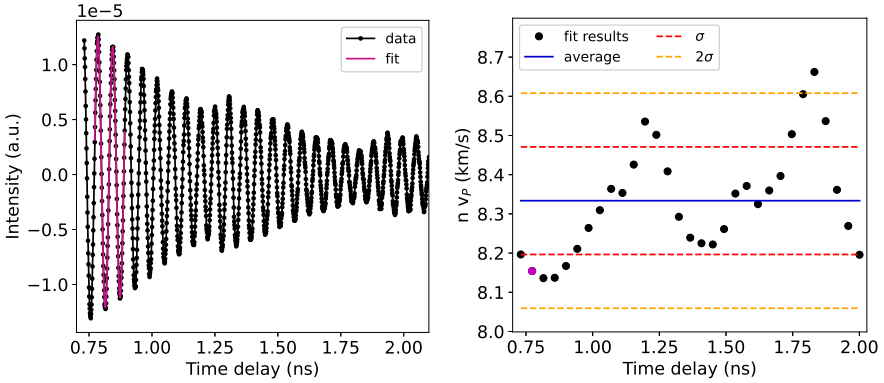


**Fig. 12**: Brillouin signal of Ar at 14.6 GPa (left panel). A fit of the signal in the window 0.773 - 0.891 ns to Equation 8 is shown in violet. The obtained $n \cdot v_P$ for each sliding window is reported in the right panel as black dots as a function of time. The violet dot corresponds to the fit shown in the left panel. The blue line indicates the average of the obtained results in the 0.75 - 2.00 ns range, which at this pressure results in $n \cdot v_P = 8.32$ km/s. Red and orange dashed lines represent $1\sigma$ and $2\sigma$ standard deviations.

The Brillouin signal can be fitted according Equation 8 in order to obtain the product of the refractive index times the longitudinal velocity $n \cdot v_P$. Note that with this technique, it is not possible to independently obtain the refractive index $n$ and the longitudinal velocity $v_P$ as a function of pressure. Performing a fit through the Brillouin oscillations on a sliding window allows

to determine whether there are multiple domains having different orientations. The fit is performed by sliding a window of 0.12 ns by steps of 0.042 ns in the range between 0.75 and 2 ns. The width of the window was chosen to fit two full periods of the sinusoidal function, and the step in order to have 30 evaluations of the velocity in the chosen range. An example of the sliding fit (the second window out of 30) is shown in the left panel of Figure 12. The obtained $n \cdot v_P$ for each window is shown in the right panel of Figure 12.

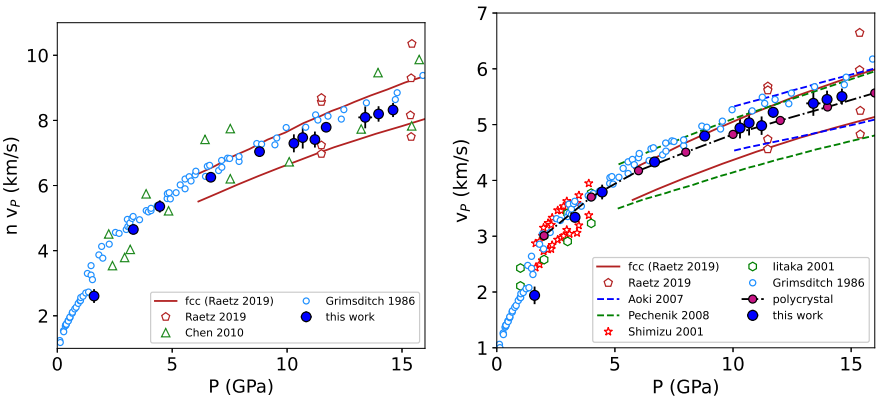


**Fig. 13**: $n \cdot v_P$ as a function of pressure measured in this work (left panel) and compared to the literature: Raetz 2019 [68], Chen 2010 [69] and Grimsditch 1986 [70]. The longitudinal velocity obtained in this work assuming the refractive index reported by Grimsditch et al. [70] is plotted in the right panel and compared to values in literature: Raetz 2019 [68], Aoki 2007 [71], Pechenik 2008 [72], Shimizu 2001 [73], Itaka 2001 [74], Grimsditch 1986 [70]. Dark red dots indicated as 'polycrystal' are the velocities of a randomly oriented Ar powder calculated assuming the density reported in Chen et al. [69] and the elastic constants $C_{ij}$ determined as the average of the sets of values reported in Raetz et al. [68, 70–72, 74].

The sliding fit procedure was performed for all collected pressure points, and the average $n \cdot v_P$ as a function of pressure are shown in the left panel of Figure 13. The uncertainty indicates the maximum and minimum values obtained in the sliding fit procedure. The here-obtained results are in good agreement with literature data. Chen et al. [69] and Raetz et al. [68] provide the velocity for two crystallographic directions [100] (slower) and [111] (faster). Our data lie in between the two, suggesting that Ar solidified as a polycrystal inside the DAC.

In the right panel of Figure 13, we report the longitudinal velocities obtained from $n \cdot v_P$ of this work, calculated assuming the refractive index from Grimsditch et al. [75]. Once again, compared to literature data, our $v_P$ falls in between the velocities of the [111] and [100] crystallographic orientations.

Velocities for a randomly oriented powder, calculated according Equation 15a, assuming the density in (Chen et al. [69] and references therein) and the elastic constants $C_{ij}$ obtained performing an average of the set of values reported in Raetz et al. [68, 70–72, 74], are reported as dark red dots. Here-measured $v_P$ are within mutual uncertainties of these estimates.

# 6 Mo: a polycrystalline foil laser heated at high pressure

The very recent installation of a laser heating system coupled to the picosecond acoustic setup broadens the range of possibilities to explore new branches of fundamental and applied physics, such as permitting the study of acoustic waves propagation in samples at the pressure and temperature conditions of planetary cores.

The feasibility of acoustics experiments depend mostly on three factors: generation, propagation and detection of the acoustic wave. As shown in Section 2, the generation strictly depends on the absorption length $\xi$ and the thermal diffusivity $D$ of the sample or, alternatively, of the transducer. The propagation of the acoustic wave is guaranteed by a low acoustic attenuation $\alpha_0$ and finally the detection depends on the reflectivity of the investigated material (or used transducer). At several thousands of K these parameters are not known and the possibility to measure an acoustic signal is, *a priori*, not obvious .

The picosecond acoustics system was upgraded to grant simultaneous generation and measurements of pressure and temperature together with measurements of thermoelastic parameters on a laser heated sample compressed in a DAC. The setup is schematically represented in Figure 14. At each side (pump or probe), the three beams are delivered to the sample and focused by the same Mitutoyo M Plan APO 20× objective. The different paths are separated according to their different wavelength by the three dichroic filters $D_1$, $D_2$ and $D_3$: the wavelength of the continuous YAG laser used for heating is 1064 nm, the blue laser for luminescence excitation is at 488 nm and the pulsed Mai Tai laser for acoustics measurements is set at 960 nm in order not to interfere with the grey body acquisition for temperature determination. The dimensions of the hot spot at sample's position can be controlled by modifying the divergence of the YAG laser beam at the entrance of the objective. The divergence is typically set to have a ∼20 $\mu$m diameter hot spot. The emitted grey body radiation is collected from a region of about 5 $\mu m$ at the center of the hot spot - there where the acoustic measurement is performed - and is delivered to a CCD detector mounted on a Czerny-Turner spectrometer.

In order to prove the feasibility of acoustic measurements at extreme pressure and temperature conditions a test experiment on a Mo foil was performed at 34 GPa, up to 2400 K. Mo was chosen for its excellent coupling with both the Mai Tai and the YAG laser, which guarantees the generation of an acoustic signal (at least at ambient temperature) and the possibility to efficiently

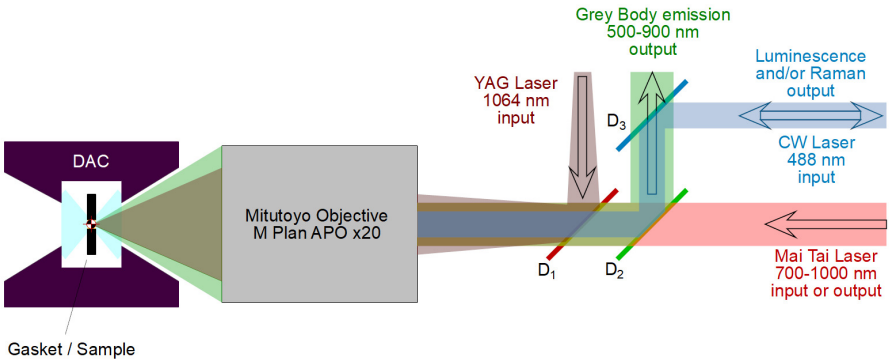


**Fig. 14**: Schematic diagram of simultaneous pressure, temperature and thermoelastic measurements on a laser heated sample compressed in a DAC. For sake of clarity, since pump and probe sides are symmetric, only one side is shown. All the optical paths are focused by a Mitutoyo M Plan APO 20× objective, depicted in grey. The Mai Tai laser beam (pump or probe) used for acoustic measurements is represented in red, the delivery of the blue laser to the DAC and the collection of the luminescence signal from the pressure sensor (e.g. ruby sphere) is shown in blue. The YAG laser delivered to the sample is represented in brown, where the spot size at the sample position is controlled by the divergence of the beam before the Mitutoyo objective. The grey body emission is collected from the hot spot and is visualized in green. $D_1$, $D_2$ and $D_3$ stand for the three dichroic filters that separate and define the different optical paths.

obtain high temperature by laser heating. Moreover, Mo has a rather simple phase diagram, with the bcc structure stable over a large pressure and temperature range[76, 77]. The measurement setup for this experiment is shown in the left panel of Figure 15. A commercial foil (Goodfellow) of a nominal thickness of 15 $\mu$m was pre-compressed between two diamonds to obtain a sample with a thickness around 3 to 5 $\mu$m and flat and reflective surfaces. The sample was then sandwiched between two disks of single-crystal $Al_2O_3$ of 23 $\mu$m thickness that served both as a pressure transmitting medium and thermal insulation. The ensemble was then loaded in a 150 $\mu$m diameter hole of a Re gasket pre-indented to 50 $\mu$m thickness and compressed thanks to a DAC equipped with diamonds of culet size of 350 $\mu$m diameter. Note that $Al_2O_3$ ensures a good quality of the sample surfaces, thus preserving a good sample reflectivity even at high pressures, but at the expenses of hydrostatic conditions.

The sample was compressed to 34 GPa and heated from both sides with the YAG laser. The arrival time of the acoustic wave was measured at the probe side at different temperatures. An example of an acoustic echo at ambient temperature conditions and for the sample heated at 1520 K is shown in the right panel of Figure 15. The emitted light from the hot spot was collected from

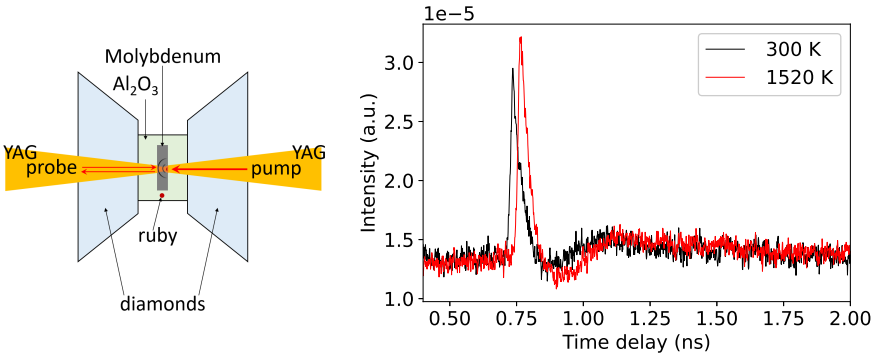


**Fig. 15**: Left panel: scheme for picosecond acoustic measurements of Mo at high pressure and high temperatures in the diamond anvil cell. The Mai Tai laser for acoustic measurements and the YAG laser for sample heating are shown in red and yellow, respectively. Note that this representation is helpful to visualize the two lasers on the sample, but it does not correspond to reality. Right panel: Time domain picosecond acoustic measurements on Mo at 34 GPa for different temperatures. The arrival time $t_1$ of the acoustic wave at the probe side of the sample is shown for measurements at ambient temperature (300 K) and at high temperature (1520 K).

the probe side of the sample, and the temperature was determined by fitting the collected intensity, normalized to the instrument transmission function, to the Planck law. An example of fit is shown in the left panel of Figure 16 for a hot spot at 1600 K.

An acoustic signal is measured at ambient temperature before heating ($t_1^i$), during laser heating at high temperature ($t_1^T$) and again at ambient temperature after heating ($t_1^f$). The temperature effect is assessed by considering the relative arrival time $t_1^{rel}$ calculated as

$$t_1^{rel} = t_1^T - \frac{t_1^i + t_1^f}{2} \quad \text{and} \quad \Delta t_1^{rel} = \frac{\mid t_1^i - t_1^f \mid}{2} \tag{17}$$

where $\Delta t_1^{rel}$ are the associated uncertainties. The obtained values as a function of the increasing temperature are shown in the right panel of Figure 16. An increase of the arrival time with temperature is in qualitative in agreement with our expectations due to the combined effect of temperature-induced reduction of sound velocities and increase in sample thickness due to thermal expansion.

This experiment unambiguously shows that, although technically more challenging, laser heating a sample with a continuous YAG laser does not prevent to perform picosecond acoustics measurements. This opens the possibility to probe acoustic signals and related properties of materials of geophysical interest under extreme conditions using a new laboratory technique.

Quantitative analysis to derive velocities as a function of pressure and temperature calls for combining travel time measurements with estimation

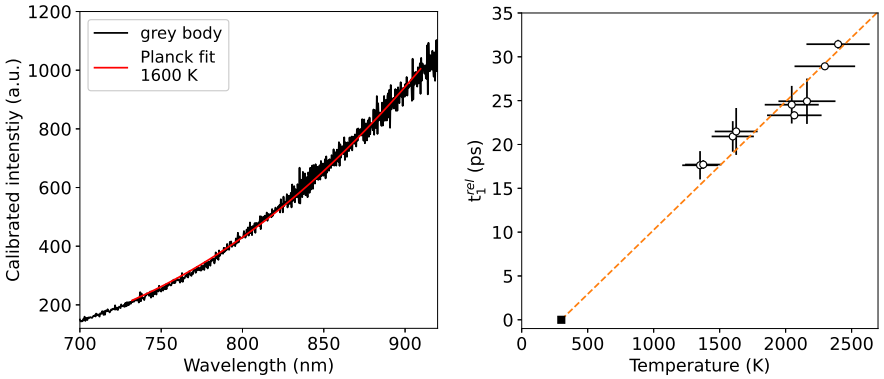


**Fig. 16**: Left panel: example of the grey body radiation emitted from the hot spot fitted to a Plank law. The temperature resulting from the fit is 1600(150) K. Right panel: relative arrival times at 34 GPa as a function of the temperature for a laser heated Mo foil. The square at 300 K is the reference and the orange dashed line serves as guide for the eyes.

of sample thickness according to a known thermal equation of state. In the literature, there is a general consensus concerning the thermal equation of state of Mo at least up to 1 Mbar [78–80]. However, in view of the possible texture induced by sample flattening between the diamonds, followed by the non-hydrostatic compression of Mo in this first test experiment, we prefer to defer this more detailed analysis to the planned experiments using a thinner foil as testing material and a sample environment that could retain the required sample surface quality also in more hydrostatic conditions (e.g. combining the use of $Al_2O_3$ substrate with gas loading).

Finally, we stress that solid-solid and solid-liquid phase transitions can be detected by the qualitative analysis of the behaviour of $t_1^{rel}$ as previously shown, as long as these transitions come with discontinuity in the volume (first order phase transitions) or at least with sudden variation of the sound velocity and/or of the thermal expansion. Picosecond acoustics thus allows to determine phase boundaries even when nothing is known on the sample properties at high pressure and temperature by the simple plot of the relative arrival times versus temperature or pressure.

# 7 Conclusions

Four scientific examples were presented here to highlight the different operating modes of the newly upgraded setup. The main motivation driving the upgrade was to extend the application of picosecond acoustics to pressures in the Mbar range coupled with temperatures exceeding 1500 K, but also to perform picosecond acoustics experiments at P-T conditions already routinely

accessible in our previous setup (e.g. [2, 7, 10–16]) on cases that could benefit from an improved acquisition speed and stability of the system.

At elevated temperature, generation and detection of a signal is more challenging. As well, acoustic attenuation leads to weaker signals and accumulation process is required for reliable data acquisition. This called for an improved stability and reproducibility of the signal generation and detection. A new design of the optical paths was required to allow high T generation by a YAG laser and the simultaneous collection of the blackbody radiation and of the luminescence and/or Raman signal of a P/T gauge, in parallel to the acoustic measurements. The new opto-mechanical solutions called for a complete rewriting of the control software. The whole upgrade led to an improved stability and reproducibility of the generation and detection of the acoustic signal, while the time required for the data acquisition has been reduced by a factor of 5. Beside being necessary for applications at high temperature, these improved performance are highly beneficial for the phonon imaging mode, as faster measurements reduce uncertainties due to uncontrolled variation, at different time scale, from fluctuations to drifts, of the P-T conditions of the sample.

Here, several different applications were shown to illustrate the current capabilities of picosecond acoustics, both in the 2D imaging and in the temporal mode. Experiments at ambient conditions and at high pressure, while in need of careful execution, do not pose anymore specific technological difficulties.

The 2D imaging mode, allowing to experimentally measure all the independent components of the elastic tensor and the sound velocities of a sample, does not require any *a priori* knowledge of the thickness. The method was shown for MgO at ambient conditions, but the same approach can be readily applied at moderate high pressures, compatible with a sample with a surface of at least 50 to 100 $\mu$m in diameter and thickness of few tenths of microns ($\sim$20 GPa). The experiment on MgO presented in this study shows that the 2D imaging mode can be used to determine elastic properties of minerals, opening the door to a wealth of possible applications in mineral-physics.

In temporal mode, experiments in Brillouin detection scheme on transparent samples were shown for two distinct cases: single-coated MgO and Ar. As well, the echoes detection mode on opaque samples is illustrated with two examples, Fe-C and Mo, where the sample thickness can be recalculated using the respective equations of state. As in all these experiments the only surface size limitation comes from the diameter of the focal spot of the pump-probe laser, and the sample thickness can be only few microns when not hundreds of nm for evaporated samples, measurements can be performed over an extended pressure range, with no intrinsic limitation other than diamond deformation, and current upper limit set by diamond breaking at $\sim$150 GPa. Accordingly, echoes can be probed for metallic samples at pressure in excess of those of the core of Mercury and Mars, and approaching the conditions of the core of the Earth. Compared to complementary laboratory techniques, picosecond acoustics can be preferred to ultrasonic interferometry for applications over a

larger pressure range, and preferred to Brillouin spectroscopy due to the faster data acquisition and the possibility to investigate opaque samples. Compared to large facility techniques such as inelastic neutron scattering, inelastic x-ray scattering or nuclear resonant inelastic x-ray scattering, picosecond acoustics is an easily accessible laboratory technique and permits systematic studies of almost any type of sample. Differently, measurements on samples laser heated in DAC, while proven feasible, still necessitate an improved experimental protocol. Indeed interpretation of arrival times measured in non-hydrostatically compressed, and hence possibly strongly textured samples, is not straightforward, and potentially misleading if not carried out with care. Nonetheless, a qualitative analysis remains pertinent when using temporal measurements to determine phase boundary.

## Acknowledgements

The authors would like to thank Marion Harmand for provision of the MgO single crystals and Antoine Boury for PVD deposition tests on MgO. The evaporation on MgO was performed by Loïc Becerra, engineer of the INSP's cleanroom, a technological platform of Sorbonne Université, and member of the network Salles Blanches Paris Centre. The authors wish to thank Eric Edmumd and Guillaume Morard for useful discussions. The authors are grateful to Nicolas Dumesnil and Charlotte Georget for their help and the machining of mechanical pieces integrated in the picosecond acoustic setup. Michel Fialin and Nicolas Rividi are acknowledged for their help during microprobe analysis. The Scanning Electron Microscope (SEM) facility at IMPMC is supported by Region Ile de France grant SESAME 2006 N I-07-593/R, INSU-CNRS, Institute de Physique (INP)–CNRS, University Pierre et Marie Curie–Paris 6, and by the French National Research Agency (ANR) grant ANR-07-BLAN-0124-01. Femtosecond laser micromachining at the Institut de Minéralogie de Physique des Matériaux et de Cosmochimie (IMPMC), Paris, has been developed and realized by the "Cellule Project" with the financial support of ANR 2010-JCJC-604- 01. This project has received funding from the European Research Council (ERC) under the European Union's Horizon 2020 research and innovation programme (Grant Agreement No. 724690).

## References

[1] Li, B., Kung, J., Liebermann, R.C.: Modern techniques in measuring elasticity of earth materials at high pressure and high temperature using ultrasonic interferometry in conjunction with synchrotron x-radiation in multi-anvil apparatus. Physics of the Earth and Planetary Interiors **143-144**, 559–574 (2004). https://doi.org/10.1016/j.pepi.2003.09.020. New Developments in High-Pressure Mineral Physics and Applications to the Earth's Interior

[2] Decremps, F., Belliard, L., Gauthier, M., Perrin, B.: Equation of state, stability, anisotropy and nonlinear elasticity of diamond-cubic (zb) silicon by phonon imaging at high pressure. Phys. Rev. B **82**, 104119 (2010). https://doi.org/10.1103/PhysRevB.82.104119

[3] Speziale, S., Marquardt, H., Duffy, T.S.: Brillouin Scattering and its Application in Geosciences. Reviews in Mineralogy and Geochemistry **78**(1), 543–603 (2014). https://doi.org/10.2138/rmg.2014.78.14

[4] Beghi, M., Every, A.G., Prakapenka, V.B., Zinin, P.V.: Synchrotron Radiation, pp. 540–612. CRC Press, ??? (2012). Chap. 10

[5] Thomsen, C., Strait, J., Vardeny, Z., Maris, H.J., Tauc, J., Hauser, J.J.: Coherent phonon generation and detection by picosecond light pulses. Phys. Rev. Lett. **53**, 989–992 (1984). https://doi.org/10.1103/PhysRevLett.53.989

[6] Threard, T., de Lima Savi, E., Avanesyan, S., Chigarev, N., Hua, Z., Tournat, V., Gusev, V.E., Hurley, D.H., Raetz, S.: Photoacoustic 3-d imaging of polycrystalline microstructure improved with transverse acoustic waves. Photoacoustics **23**, 100286 (2021). https://doi.org/10.1016/j.pacs.2021.100286

[7] Decremps, F., Antonangeli, D., Gauthier, M., Ayrinhac, S., Morand, M., Marchand, G.L., Bergame, F., Philippe, J.: Sound velocity of iron up to 152 gpa by picosecond acoustics in diamond anvil cell. Geophysical Research Letters **41**(5), 1459–1464 (2014) https://arxiv.org/abs/https://agupubs.onlinelibrary.wiley.com/doi/pdf/10.1002/2013GL058859. https://doi.org/10.1002/2013GL058859

[8] Goncharov, A.F., Gauthier, M., Antonangeli, D., Ayrinhac, S., Decremps, F., Morand, M., Grechnev, A., Tretyak, S.M., Freiman, Y.A.: Elasticity and poisson's ratio of hexagonal close-packed hydrogen at high pressures. Phys. Rev. B **95**, 214104 (2017). https://doi.org/10.1103/PhysRevB.95.214104

[9] Wakamatsu, T., Ohta, K., Yagi, T., Hirose, K., Ohishi, Y.: Measurements of sound velocity in iron-nickel alloys by femtosecond laser pulses in a diamond anvil cell. Physics and Chemistry of Minerals **45**(6), 589–595 (2018). https://doi.org/10.1007/s00269-018-0944-3

[10] Edmund, E., Antonangeli, D., Decremps, F., Morard, G., Ayrinhac, S., Gauthier, M., Boulard, E., Mezouar, M., Hanfland, M., Guignot, N.: Structure and elasticity of cubic fe-si alloys at high pressures. Phys. Rev. B **100**, 134105 (2019). https://doi.org/10.1103/PhysRevB.100.134105

[11] Edmund, E., Gauthier, M., Antonangeli, D., Ayrinhac, S., Boccato, S.,

Deletang, T., Morand, M., Garino, Y., Parisiades, P., Decremps, F.: Picosecond acoustics technique to measure the sound velocities of fe-si alloys and si single-crystals at high pressure. Minerals **10**(3) (2020). https://doi.org/10.3390/min10030214

[12] Decremps, F., Belliard, L., Couzinet, B., Vincent, S., Munsch, P., Le Marchand, G., Perrin, B.: Liquid mercury sound velocity measurements under high pressure and high temperature by picosecond acoustics in a diamond anvils cell. Review of Scientific Instruments **80**(7), 073902 (2009). https://doi.org/10.1063/1.3160104

[13] Ayrinhac, S., Gauthier, M., Bove, L.E., Morand, M., Le Marchand, G., Bergame, F., Philippe, J., Decremps, F.: Equation of state of liquid mercury to 520 k and 7 gpa from acoustic velocity measurements. The Journal of Chemical Physics **140**(24), 244201 (2014). https://doi.org/10.1063/1.4882695

[14] Ayrinhac, S., Gauthier, M., Le Marchand, G., Morand, M., Bergame, F., Decremps, F.: Thermodynamic properties of liquid gallium from picosecond acoustic velocity measurements. Journal of Physics: Condensed Matter **27**(27), 275103 (2015). https://doi.org/10.1088/0953-8984/27/27/275103

[15] Ayrinhac, S., Robinson, V.N., Decremps, F., Gauthier, M., Antonangeli, D., Scandolo, S., Morand, M.: High-pressure transformations in liquid rubidium. Phys. Rev. Materials **4**, 113611 (2020). https://doi.org/10.1103/PhysRevMaterials.4.113611

[16] Decremps, F., Ayrinhac, S., Gauthier, M., Antonangeli, D., Morand, M., Garino, Y., Parisiades, P.: Sound velocity and equation of state in liquid cesium at high pressure and high temperature. Phys. Rev. B **98**, 184103 (2018). https://doi.org/10.1103/PhysRevB.98.184103

[17] Antonangeli, D., Ohtani, E.: Sound velocity of hcp-Fe at high pressure: experimental constraints, extrapolations and comparison with seismic models. Progress in Earth and Planetary Science **2**(3), 2197–4284 (2015). https://doi.org/10.1186/s40645-015-0034-9

[18] Murphy, C.A., Jackson, J.M., Sturhahn, W.: Experimental constraints on the thermodynamics and sound velocities of hcp-fe to core pressures. Journal of Geophysical Research: Solid Earth **118**(5), 1999–2016 (2013) https://arxiv.org/abs/https://agupubs.onlinelibrary.wiley.com/doi/pdf/10.1002/jgrb.50166. https://doi.org/10.1002/jgrb.50166

[19] Gleason, A.E., Mao, W.L., Zhao, J.: Sound velocities for hexagonally close-packed iron compressed hydrostatically to 136 gpa from phonon density of states. Geophysical Research Letters **40**, 2983–2987 (2013)

[20] Antonangeli, D., Siebert, J., Badro, J., Farber, D.L., Fiquet, G., Morard, G., Ryerson, F.J.: Composition of the Earth's inner core from high-pressure sound velocity measurements in Fe - Ni - Si alloys. Earth and Planetary Science Letters **295**(1-2), 292–296 (2010)

[21] Antonangeli, D., Komabayashi, T., Occelli, F., Borissenko, E., Fiquet, G., Fei, Y., Walters, A.C.: Simultaneous sound velocity and density measurements of hcp iron up to 93 GPa and 1100 K: An experimental test of the Birch's law at high temperature. Earth and Planetary Science Letters **331**, 210–214 (2012). https://doi.org/10.1016/j.epsl.2012.03.024

[22] Sakamaki, T., Ohtani, E., Fukui, H., Kamada, S., Takahashi, S., Sakairi, T., Takahata, A., Sakai, T., Tsutsui, S., Ishikawa, D., Shiraishi, R., Seto, Y., Tsuchiya, T., Baron, A.Q.R.: Constraints on earth’s inner core composition inferred from measurements of the sound velocity of hcp-iron in extreme conditions. Science Advances **2**(2), 1500802 (2016). https://doi.org/10.1126/sciadv.1500802

[23] Antonangeli, D., Morard, G., Paolasini, L., Garbarino, G., Murphy, C.A., Edmund, E., Decremps, F., Fiquet, G., Bosak, A., Mezouar, M., Fei, Y.: Sound velocities and density measurements of solid hcp-fe and hcp-fe-si (9 wt.%) alloy at high pressure: Constraints on the si abundance in the earth's inner core. Earth and Planetary Science Letters **482**, 446–453 (2018). https://doi.org/10.1016/j.epsl.2017.11.043

[24] Antonangeli, D., Krisch, M., Farber, D.L., Ruddle, D.G., Fiquet, G.: Elasticity of hexagonal-closed-packed cobalt at high pressure and temperature: A quasiharmonic case. Phys. Rev. Lett. **100**, 085501 (2008). https://doi.org/10.1103/PhysRevLett.100.085501

[25] Antonangeli, D., Siebert, J., Aracne, C.M., Farber, D.L., Bosak, A., Hoesch, M., Krisch, M., Ryerson, F.J., Fiquet, G., Badro, J.: Spin crossover in ferropericlase at high pressure: A seismologically transparent transition? Science **331**(6013), 64–67 (2011). https://doi.org/10.1126/science.1198429

[26] Antonangeli, D., Farber, D.L., Bosak, A., Aracne, C.M., Ruddle, D.G., Krisch, M.: Phonon triggered rhombohedral lattice distortion in vanadium at high pressure . Scientific Reports **6**(31887), 2045–2322 (2016). https://doi.org/10.1038/srep31887

[27] Chigarev, N., Zinin, P., Mounier, D., Bulou, A., Ming, L.C., Acosta, T., Gusev, V.: Analysis of ultrasonic echoes induced by pulsed laser action on an iron film in a diamond anvil cell. High Pressure Research **30**(1), 78–82 (2010). https://doi.org/10.1080/08957950903549519

[28] Zinin, P.V., Prakapenka, V.B., Burgess, K., Odake, S., Chigarev, N.,

Sharma, S.K.: Combined laser ultrasonics, laser heating, and raman scattering in diamond anvil cell system. Review of Scientific Instruments **87**(12), 123908 (2016). https://doi.org/10.1063/1.4972588

[29] Dziewonski, A.M., Anderson, D.L.: Preliminary reference Earth model. Physics of the Earth and Planetary Interiors **25**, 297 (1981)

[30] Anzellini, S., Dewaele, A., Mezouar, M., Loubeyre, P., Morard, G.: Melting of iron at Earth's inner core boundary based on fast X-ray diffraction. Science **340**(6131), 464–6 (2013)

[31] Morard, G., Andrault, D., Antonangeli, D., Nakajima, Y., Auzende, A.L., Boulard, E., Cervera, S., Clark, A., Lord, O.T., Siebert, J., Svitlyk, V., Garbarino, G., Mezouar, M.: Fe-FeO and Fe-Fe3C melting relations at Earth's core-mantle boundary conditions: Implications for a volatile-rich or oxygen-rich core. Earth and Planetary Science Letters **473**, 94–103 (2017)

[32] Anzellini, S., Boccato, S.: A practical review of the laser-heated diamond anvil cell for university laboratories and synchrotron applications. Crystals **10**(6) (2020). https://doi.org/10.3390/cryst10060459

[33] Andrault, D., Monteux, J., Le Bars, M., Samuel, H.: The deep earth may not be cooling down. Earth and Planetary Science Letters **443**, 195–203 (2016). https://doi.org/10.1016/j.epsl.2016.03.020

[34] Decremps, F., Gauthier, M., Ayrinhac, S., Bove, L., Belliard, L., Perrin, B., Morand, M., Le Marchand, G., Bergame, F., Philippe, J.: Picosecond acoustics method for measuring the thermodynamical properties of solids and liquids at high pressure and high temperature. Ultrasonics **56**, 129–140 (2015). https://doi.org/10.1016/j.ultras.2014.04.011

[35] Matsuda, O., Larciprete, M.C., Li Voti, R., Wright, O.B.: Fundamentals of picosecond laser ultrasonics. Ultrasonics **56**, 3–20 (2015). https://doi.org/10.1016/j.ultras.2014.06.005

[36] Grahn, H.T., Maris, H.J., Tauc, J.: Picosecond ultrasonics. IEEE Journal of Quantum Electronics **25**(12), 2562–2569 (1989). https://doi.org/10.1109/3.40643

[37] McPeak, K.M., Jayanti, S.V., Kress, S.J.P., Meyer, S., Iotti, S., Rossinelli, A., Norris, D.J.: Plasmonic films can easily be better: Rules and recipes. ACS Photonics **2**(3), 326–333 (2015). https://doi.org/10.1021/ph5004237

[38] Royer, D., Dieulesaint, E.: Elastic Waves in Solids I: Free and Guided Propagation. Springer, Paris (1999)

[39] Press, W.H., Teukolsky, S.A., Vetterling, W.T., Flannery, B.P.: Numerical Recipes: The Art of Scientific Computing (3rd Ed.). Cambridge University Press., New York (2007)

[40] McSkimin, H.J., Bond, W.L., Buehler, E., Teal, G.K.: Measurement of the elastic constants of silicon single crystals and their thermal coefficients. Phys. Rev. **83**, 1080–1080 (1951). https://doi.org/10.1103/PhysRev.83.1080

[41] McSkimin, H.J.: Measurement of elastic constants at low temperatures by means of ultrasonic waves data for silicon and germanium single crystals, and for fused silica. Journal of Applied Physics **24**(8), 988–997 (1953). https://doi.org/10.1063/1.1721449

[42] McSkimin, H.J., Andreatch, P.: Elastic moduli of silicon vs hydrostatic pressure at 25.0 c and 195.8 c. Journal of Applied Physics **35**(7), 2161–2165 (1964). https://doi.org/10.1063/1.1702809

[43] Liebermann, R.C.: Multi-anvil, high pressure apparatus: a half-century of development and progress. High Pressure Research **31**(4), 493–532 (2011). https://doi.org/10.1080/08957959.2011.618698

[44] Sinogeikin, S.V., Bass, J.D.: Single-crystal elasticity of pyrope and mgo to 20 gpa by brillouin scattering in the diamond cell. Physics of the Earth and Planetary Interiors **120**(1), 43–62 (2000). https://doi.org/10.1016/S0031-9201(00)00143-6

[45] Ito, E., Takahashi, E.: Postspinel transformations in the system mg2sio4-fe2sio4 and some geophysical implications. Journal of Geophysical Research: Solid Earth **94**(B8), 10637–10646 (1989) https://arxiv.org/abs/https://agupubs.onlinelibrary.wiley.com/doi/pdf/10.1029/JB094iB08p10637. https://doi.org/10.1029/JB094iB08p10637

[46] Bina, C.R., Silver, P.G.: Constraints on lower mantle composition and temperature from density and bulk sound velocity profiles. Geophysical Research Letters **17**(8), 1153–1156 (1990) https://arxiv.org/abs/https://agupubs.onlinelibrary.wiley.com/doi/pdf/10.1029/GL017i008p01153. https://doi.org/10.1029/GL017i008p01153

[47] Zhao, Y., Anderson, D.L.: Mineral physics constraints on the chemical composition of the earth's lower mantle. Physics of the Earth and Planetary Interiors **85**(3), 273–292 (1994). https://doi.org/10.1016/0031-9201(94)90118-X

[48] Sinogeikin, S.V., Jackson, J.M., O'Neill, B., Palko, J.W., Bass, J.D.: Compact high-temperature cell for brillouin scattering measurements. Review of Scientific Instruments **71**(1), 201–206 (2000). https://doi.org/10.1063/

1.1150183

[49] Kono, Y., Irifune, T., Higo, Y., Inoue, T., Barnhoorn, A.: P v t relation of mgo derived by simultaneous elastic wave velocity and in situ x-ray measurements: A new pressure scale for the mantle transition region. Physics of the Earth and Planetary Interiors **183**(1), 196–211 (2010). https://doi.org/10.1016/j.pepi.2010.03.010. Special Issue on Deep Slab and Mantle Dynamics

[50] Stephens, R., Malitson, I.: Index of Refraction of Magnesium Oxide. Journal of Research of the National Bureau of Standards **49**, 249–252 (1952)

[51] Zha, C.-S., Mao, H.-k., Hemley, R.J.: Elasticity of mgo and a primary pressure scale to 55 gpa. Proceedings of the National Academy of Sciences **97**(25), 13494–13499 (2000) https://arxiv.org/abs/https://www.pnas.org/content/97/25/13494.full.pdf. https://doi.org/10.1073/pnas.240466697

[52] Calderon, E., Gauthier, M., Decremps, F., Hamel, G., Syfosse, G., Polian, A.: Complete determination of the elastic moduli of alpha-quartz under hydrostatic pressure up to 1 gpa: an ultrasonic study. Journal of Physics: Condensed Matter **19**, 1–13 (2007). https://doi.org/10.1088/0953-8984/19/43/436228

[53] Nye, J.: Physical Properties of Crystals: Their Representation by Tensors and Matrices. Oxford Science Publications, Oxford (1985)

[54] Klotz, S., Chervin, J.-C., Munsch, P., Le Marchand, G.: Hydrostatic limits of 11 pressure. Journal of Physics D: Applied Physics **42**, 075413 (2009). https://doi.org/10.1088/0022-3727/42/7/075413

[55] Zhang, J., Guyot, F.: Thermal equation of state of iron and fe0.91si0.09. Physics and Chemistry of Minerals **26**, 206 (1999). https://doi.org/10.1007/s002690050178

[56] Gao, L., Chen, B., Wang, J., Alp, E.E., Zhao, J., Lerche, M., Sturhahn, W., Scott, H.P., Huang, F., Ding, Y., Sinogeikin, S.V., Lundstrom, C.C., Bass, J.D., Li, J.: Pressure-induced magnetic transition and sound velocities of fe3c: Implications for carbon in the earth's inner core. Geophysical Research Letters **35**(17) (2008) https://arxiv.org/abs/https://agupubs.onlinelibrary.wiley.com/doi/pdf/10.1029/2008GL034817. https://doi.org/10.1029/2008GL034817

[57] Mao, H.K., Xu, J., Struzhkin, V.V., Shu, J., Hemley, R.J., Sturhahn, W., Hu, M.Y., Alp, E.E., Vocadlo, L., Alfe, D., Price, G.D., Gillan, M.J., Schwoerer-Bohning, M., Hausermann, D., Eng, P., Shen, G., Giefers, H.,

Lubbers, R., Wortmann, G.: Phonon density of states of iron up to 153 gigapascals. Science **292**(5518), 914–916 (2001). https://doi.org/10.1126/science.1057670

[58] Fiquet, G., Badro, J., Guyot, F., Requardt, H., Krisch, M.: Sound velocities in iron to 110 gigapascals. Science **291**(5503), 468–471 (2001). https://doi.org/10.1126/science.291.5503.468

[59] Chen, B., Lai, X., Li, J., Liu, J., Zhao, J., Bi, W., Ercan Alp, E., Hu, M.Y., Xiao, Y.: Experimental constraints on the sound velocities of cementite fe3c to core pressures. Earth and Planetary Science Letters **494**, 164–171 (2018). https://doi.org/10.1016/j.epsl.2018.05.002

[60] Mookherjee, M.: Elasticity and anisotropy of Fe3C at high pressures. American Mineralogist **96**(10), 1530–1536 (2011) https://arxiv.org/abs/https://pubs.geoscienceworld.org/msa/ammin/article-pdf/96/10/1530/3629841/14_3917MookherjeeOC.pdf. https://doi.org/10.2138/am.2011.3917

[61] Gao, L., Chen, B., Zhao, J., Alp, E.E., Sturhahn, W., Li, J.: Effect of temperature on sound velocities of compressed fe3c, a candidate component of the earth's inner core. Earth and Planetary Science Letters **309**(3), 213–220 (2011). https://doi.org/10.1016/j.epsl.2011.06.037

[62] Gao, L., Chen, B., Lerche, M., Alp, E.E., Sturhahn, W., Zhao, J., Yavaş, H., Li, J.: Sound velocities of compressed $Fe_3C$ from simultaneous synchrotron X-ray diffraction and nuclear resonant scattering measurements. Journal of Synchrotron Radiation **16**(6), 714–722 (2009). https://doi.org/10.1107/S0909049509033731

[63] Fiquet, G., Badro, J., Gregoryanz, E., Fei, Y., Occelli, F.: Sound velocity in iron carbide (fe3c) at high pressure: Implications for the carbon content of the earth's inner core. Physics of the Earth and Planetary Interiors **172**(1), 125–129 (2009). https://doi.org/10.1016/j.pepi.2008.05.016. Diffusion, deformation and mineral properties of the Earth's interior. A Special Volume to honour the scientific contribution of Professor Olivier Jaoul

[64] Chen, B., Li, Z., Zhang, D., Liu, J., Hu, M.Y., Zhao, J., Bi, W., Alp, E.E., Xiao, Y., Chow, P., Li, J.: Hidden carbon in earth's inner core revealed by shear softening in dense fe7c3. Proceedings of the National Academy of Sciences **111**(50), 17755–17758 (2014) https://arxiv.org/abs/https://www.pnas.org/content/111/50/17755.full.pdf. https://doi.org/10.1073/pnas.1411154111

[65] Mookherjee, M., Nakajima, Y., Steinle-Neumann, G., Glazyrin, K.,

Wu, X., Dubrovinsky, L., McCammon, C., Chumakov, A.: High-pressure behavior of iron carbide (fe7c3) at inner core conditions. Journal of Geophysical Research: Solid Earth **116**(B4) (2011) https://arxiv.org/abs/https://agupubs.onlinelibrary.wiley.com/doi/pdf/10.1029/2010JB007819. https://doi.org/10.1029/2010JB007819

[66] Pamato, M.G., Li, Y., Antonangeli, D., Miozzi, F., Morard, G., Wood, I.G., Vocadlo, L., Brodholt, J.P., Mezouar, M.: Equation of state of hcp fe-c-si alloys and the effect of c incorporation mechanism on the density of hcp fe alloys at 300Å k. Journal of Geophysical Research: Solid Earth **125**(12), 2020–020159 (2020) https://arxiv.org/abs/https://agupubs.onlinelibrary.wiley.com/doi/pdf/10.1029/2020JB020159. https://doi.org/10.1029/2020JB020159

[67] Datchi, F., Loubeyre, P., LeToullec, R.: Extended and accurate determination of the melting curves of argon, helium, ice ($h_2O$), and hydrogen ($h_2$). Phys. Rev. B **61**, 6535–6546 (2000). https://doi.org/10.1103/PhysRevB.61.6535

[68] Raetz, S., Kuriakose, M., Djemia, P., Nikitin, S.M., Chigarev, N., Tournat, V., Bulou, A., Lomonosov, A., Gusev, V.E., Zerr, A.: Elastic anisotropy and single-crystal moduli of solid argon up to 64 gpa from time-domain brillouin scattering. Phys. Rev. B **99**, 224102 (2019). https://doi.org/10.1103/PhysRevB.99.224102

[69] Chen, B., Gleason, A.E., Yan, J.Y., Koski, K.J., Clark, S., Jeanloz, R.: Elasticity, strength, and refractive index of argon at high pressures. Phys. Rev. B **81**, 144110 (2010). https://doi.org/10.1103/PhysRevB.81.144110

[70] Grimsditch, M., Loubeyre, P., Polian, A.: Brillouin scattering and three-body forces in argon at high pressures. Phys. Rev. B **33**, 7192–7200 (1986). https://doi.org/10.1103/PhysRevB.33.7192

[71] Aoki, M., Kurokawa, T.: A simple environment-dependent overlap potential and cauchy violation in solid argon. Journal of Physics: Condensed Matter **19**(23), 236228 (2007). https://doi.org/10.1088/0953-8984/19/23/236228

[72] Pechenik, E., Kelson, I., Makov, G.: Many-body model of rare gases at high pressures. Phys. Rev. B **78**, 134109 (2008). https://doi.org/10.1103/PhysRevB.78.134109

[73] Shimizu, H., Tashiro, H., Kume, T., Sasaki, S.: High-pressure elastic properties of solid argon to 70 gpa. Phys. Rev. Lett. **86**, 4568–4571 (2001). https://doi.org/10.1103/PhysRevLett.86.4568

[74] Iitaka, T., Ebisuzaki, T.: First-principles calculation of elastic properties

of solid argon at high pressures. Phys. Rev. B **65**, 012103 (2001). https://doi.org/10.1103/PhysRevB.65.012103

[75] Grimsditch, M., Letoullec, R., Polian, A., Gauthier, M.: Refractive index determination in diamond anvil cells: Results for argon. Journal of Applied Physics **60**(10), 3479–3481 (1986). https://doi.org/10.1063/1.337597

[76] Belonoshko, A.B., Simak, S.I., Kochetov, A.E., Johansson, B., Burakovsky, L., Preston, D.L.: High-pressure melting of molybdenum. Phys. Rev. Lett. **92**, 195701 (2004). https://doi.org/10.1103/PhysRevLett.92.195701

[77] Baty, S., Burakovsky, L., Preston, D.: Topological equivalence of the phase diagrams of molybdenum and tungsten. Crystals **10**(1) (2020). https://doi.org/10.3390/cryst10010020

[78] Dorogokupets, P.I., Sokolova, T.S., Danilov, B.S., Litasov, K.D.: Near-absolute equations of state of diamond, ag, al, au, cu, mo, nb, pt, ta, and w for quasi-hydrostatic conditions. Geodyn. Tectonophysics. **3**, 129–166 (2012)

[79] Litasov, K.D., Dorogokupets, P.I., Ohtani, E., Fei, Y., Shatskiy, A., Sharygin, I.S., Gavryushkin, P.N., Rashchenko, S.V., Seryotkin, Y.V., Higo, Y., Funakoshi, K., Chanyshev, A.D., Lobanov, S.S.: Thermal equation of state and thermodynamic properties of molybdenum at high pressures. Journal of Applied Physics **113**(9), 093507 (2013). https://doi.org/10.1063/1.4794127

[80] Akhmedov, E.N.: Molybdenum lattice properties at high pressure. Journal of Physics and Chemistry of Solids **121**, 62–66 (2018). https://doi.org/10.1016/j.jpcs.2018.05.011